Realistic finite-temperature effects in neutron star merger simulations

Carolyn A. Raithel, 1,2,3,* Vasileios Paschalidis, 4,5 and Feryal Özel School of Natural Sciences, Institute for Advanced Study,

1 Einstein Drive, Princeton, New Jersey 08540, USA

Princeton Center for Theoretical Science, Jadwin Hall, Princeton University,

Princeton, New Jersey 08540, USA

Princeton Gravity Initiative, Jadwin Hall, Princeton University, Princeton, New Jersey 08540, USA

Department of Astronomy and Steward Observatory, University of Arizona,

933 N. Cherry Avenue, Tucson, Arizona 85721, USA

Department of Physics, University of Arizona, 1118 E. Fourth Street, Arizona 85721, USA

(Received 17 April 2021; accepted 3 August 2021; published 14 September 2021)

Binary neutron star mergers provide a unique probe of the dense-matter equation of state (EoS) across a wide range of parameter space, from the zero-temperature EoS during the inspiral to the high-temperature EoS following the merger. In this paper, we implement a new model for calculating parametrized finite-temperature EoS effects into numerical relativity simulations. This " M^* -model" is based on a two-parameter approximation of the particle effective mass and includes the leading-order effects of degeneracy in the thermal pressure and energy. We test our numerical implementation by performing evolutions of rotating single stars with zero- and nonzero temperature gradients, as well as evolutions of binary neutron star mergers. We find that our new finite-temperature EoS implementation can support stable stars over many dynamical timescales. We also perform a first parameter study to explore the role of the M^* parameters in binary neutron star merger simulations. All simulations start from identical initial data with identical cold EoSs, and differ only in the thermal part of the EoS. We find that both the thermal profile of the remnant and the postmerger gravitational wave signal depend on the choice of M^* parameters, but that the total merger ejecta depends only weakly on the finite-temperature part of the EoS across a wide range of parameters. Our simulations provide a first step toward understanding how the finite-temperature properties of dense matter may affect future observations of binary neutron star mergers.

DOI: 10.1103/PhysRevD.104.063016

I. INTRODUCTION

With the recent detections of gravitational waves from multiple likely neutron star-neutron star (NSNS) mergers [1,2], we are now in a new era of gravitational wave and multimessenger astronomy. Already, these gravitational waves have been used to constrain the properties of the dense nuclear matter contained in the neutron star interior [see, e.g., [3–5], for recent reviews]. Because the LIGO-Virgo sensitivity is highest for frequencies ≲1 kHz, the main gravitational wave information detected so far comes from the binary inspiral, during which neutron stars are expected to remain thermodynamically cold. As a result, all analyses of LIGO-Virgo events to date have specifically constrained the equation of state (EoS) at effectively zero temperature.

Following the merger, shock heating is expected to raise the temperature of the system to 10–100 MeV [e.g., [6,7], for reviews], which is well above the Fermi energy of the matter. At such temperatures, the thermal pressure can

make up a significant fraction of the total pressure and can thus influence the structure of the merger remnant. This, in turn, has been shown to affect a wide range of NSNS merger properties, from the lifetime of the merger remnant to the postmerger gravitational wave (GW) spectrum and the amounts of matter ejected [e.g., [8–13]]. As a result, observation of these postmerger properties could provide a new probe into the EoS at *finite temperature*.

While a large number of cold, neutron star EoSs have been calculated in the zero-temperature limit [for reviews, see [14,15]], there exists a much smaller number of EoSs that are self-consistently calculated at nonzero temperatures. These finite-temperature EoSs include the well-known LS model, which is based on a compressible liquid drop model of nuclei [16], and the STOS model, which was calculated using relativistic mean field theory with a Thomas-Fermi approximation [17]. Another ~10 models have been calculated using a statistical model developed by Hempel and Schaffner-Bielich [18] for different relativistic mean field models and nuclear mass tables, spanning a wider range of neutron star properties. Additionally, the Compose online directory for neutron star EoS tables has

^{*}craithel@ias.edu

provided a pathway for groups to easily publish finite-temperature EoS tables as they become available, and has further increased the number of available models [19] (for a recent review of finite-temperature EoSs, see [20]).

Despite these efforts, the total number of publiclyavailable finite-temperature EoS models remains relatively small and they do not span the full range of possible densematter physics. In addition, some models are not consistent with modern astrophysical constraints. For example, several of the finite-temperature EoS tables predict cold neutron star radii of ≥13 km (e.g., the NL3, TM1, DD2, and TMA EoSs; see, e.g., Table 1 of [21] and references therein), which are in tension with the latest constraints inferred from LMXB observations and from GW170817 [3,4,15]. Critically, there is currently no implementation of a framework where one can attach a realistic thermal model to any underlying cold nuclear EoS, since all existing finite-temperature EoS tables have already assumed a particular cold component. Having an analytic, parametric framework for the thermal physics would be necessary if we hope to one day infer the properties of finite-temperature matter from neutron star merger observations. Finally, compared to an analytic framework, these tabulated EoSs add an extra computational expense to already-expensive numerical simulations.

In order to span a larger range of underlying physics at a low computational cost, many authors have turned, instead, to an ad-hoc and analytic approach, in which the energy density, ϵ , and pressure, P, are decomposed according to

$$\epsilon = \epsilon_{\text{cold}} + \epsilon_{\text{th}}$$
 (1a)

$$P = P_{\text{cold}} + P_{\text{th}}, \tag{1b}$$

where the subscript "cold" indicates that the thermodynamic quantity is calculated at zero-temperature, while the subscript "th" indicates the thermal contribution to that quantity. The cold component can be a microphysical EoS or an agnostic parameterization, and is typically assumed to be in β -equilibrium. A thermal correction is then added to the cold component, in order to allow for shock heating in the system. In the so-called "hybrid" approach, which was first introduced in [22] and is now widely used, the thermal correction is approximated as

$$P_{\rm th} = \epsilon_{\rm th}(\Gamma_{\rm th} - 1),\tag{2}$$

where the thermal index, Γ_{th} , is assumed to be constant with a value that is independent of the cold EoS.

In certain regimes, such as for an ideal fluid or for a gas of relativistic particles, the thermal index is indeed constant. In fact, the values of Γ_{th} that are commonly used in recent binary neutron star simulations, $\Gamma_{th} \in [1.5,2]$, are approximately consistent with an ideal-fluid EoS, for which $\Gamma_{th} = 5/3$. This is why the hybrid approach is sometimes referred to as an ideal-fluid approximation. However, for

the degenerate matter that is expected to be found in the cores of neutron stars, Γ_{th} has a strong density dependence, which is neglected in this hybrid approach [see, e.g., [23]]. By neglecting the effects of degeneracy, the hybrid approach has been shown to overestimate the thermal pressure by up to four orders of magnitude at densities of interest [24], and can introduce significant shifts into the postmerger gravitational wave frequencies found in NSNS simulations [10,25].

Within Landau's Fermi liquid theory, the densitydependence of Γ_{th} can be written directly in terms of the particle effective mass [26,27]. Using this fact, the authors in [24] (hereafter RÖP) introduced a framework for calculating finite-temperature effects based on a new parametrization of the particle effective mass, which is referred to as the M^* -approximation. This two-parameter model allows for a robust calculation of the thermal pressure including the leading-order effects of degeneracy, while still keeping the flexibility of Eqs. (1a)–(1b). As with the hybrid approach, the M^* -approximation of the thermal pressure can be added to any cold EoS, whether it is microphysical or parametric in nature. This framework for calculating the EoS at arbitrary temperatures and proton fractions was found to closely approximate the results of a large family of EoS tables, with errors of ≤30% in the thermal pressure at densities of interest (cf. the four ordersof-magnitude errors of the hybrid approach) [24].

While Fermi liquid theory is a useful approach to calculating thermal effects in dense matter, non-Fermi liquid effects [28] can be important in some neutron star settings. For example, such effects can lead to corrections to the specific heat [29], neutrino emissivity [30], and bulk viscosity [31] of degenerate, ungapped quark matter. Fermi liquid theory also cannot describe the formation of bound states, such as the nuclei that form at densities below $0.5 n_{\text{sat}}$ [32]. Accordingly, in the M^* -framework of RÖP, the matter is assumed to be nucleonic and the presence of nuclei at low densities and temperatures is neglected. We note, however, that in the numerical implementation in the present paper, the nuclei are neglected in such a way that this simplification effectively cancels out, and we nevertheless recover the correct description of the pressure and energy at low densities (see the Appendix A).

Although other frameworks for calculating the EoS in terms of the particle effective mass have been proposed [e.g., [33–38]], these models depend on a much larger number of parameters, which dramatically increases the computational cost of exploring their parameter spaces with NSNS merger simulations. By capturing the relevant thermal physics with just two free parameters, the M^* -approximation makes it computationally possible to study the role of each parameter in merger simulations in full numerical relativity. Additionally, because the M^* -approximation can be combined with any cold EoS, it becomes possible to explore any part of the full EoS parameter space within this framework.

In this paper, we implement the M^* -framework for calculating finite-temperature effects into neutron star merger simulations in full general relativity. We test the implementation and performance of the M^* -framework in evolutions of isolated rotating stars in equilibrium, with both zero and nonzero initial temperature profiles, as well as in full evolutions of NSNS mergers. In all cases, we find that our implementation of the M^* -framework maintains the stable equilibrium of stars over many dynamical timescales. We also perform a parameter study to explore the range of outcomes from select NSNS mergers with different values of M^* -parameters. In particular, we study four sets of M^* -parameters which span a broad range of possible nuclear physics, and we compare the evolutions with these M^* -parameters to evolutions with constant values of Γ_{th} , to demonstrate the differences between the M^* - and hybrid approaches. We find that the inspiral phase and the time to merger are unaffected by the choice of M^* -parameters, but that the thermal profile of the remnant and the postmerger GW signal are both sensitive to finite-temperature effects. We find no numerically significant difference in the total amounts of matter ejected for the various M^* -parameters explored in this work, although the ejecta can be a factor of a few lower for $\Gamma_{\rm th}=2$, compared to any of the M^* evolutions or the hybrid evolution with $\Gamma_{th} = 1.5$.

The structure of the paper is as follows: We start in Sec. II with a brief discussion of the current uncertainties in the finite-temperature EoS. Section III presents an overview of the tests performed in this paper. In Sec. IV, we discuss the numerical methods used in our simulations, with the implementation of the M^* -framework discussed in detail in Sec. IV A. Finally, in Sec. V, we present the results from the NSNS merger simulations, and we discuss how different assumptions about the thermal physics affect various merger properties. Convergence tests and resolution studies can be found in Appendixes B and C. Unless otherwise specified, we adopt geometrized units in which G = c = 1.

II. UNCERTAINTIES IN THE FINITE-TEMPERATURE EOS FOR DENSE NUCLEAR MATTER

Existing finite-temperature EoS tables remain quite uncertain at the supranuclear densities and high temperatures relevant to binary neutron star mergers. The range of thermal pressures predicted by a sample of commonly used finite-temperature EoSs is shown in Fig. 1. These EoSs include the DD2, TMA, TM1, FSG models calculated within the statistical framework of Hempel and Schaffner-Bielich [18] (and references therein), SFHo and SFHx [39], NL3 and FSU [40], and the LS220 model of Lattimer and Swesty [16]. The top panel shows the thermal pressure relative to the cold pressure, for matter at a temperature of $k_BT = 20$ MeV and proton fraction $Y_e = 0.1$. We note that the "cold" pressure corresponds to $k_BT = 0.1$ MeV, which is among the lowest reliable temperatures from the

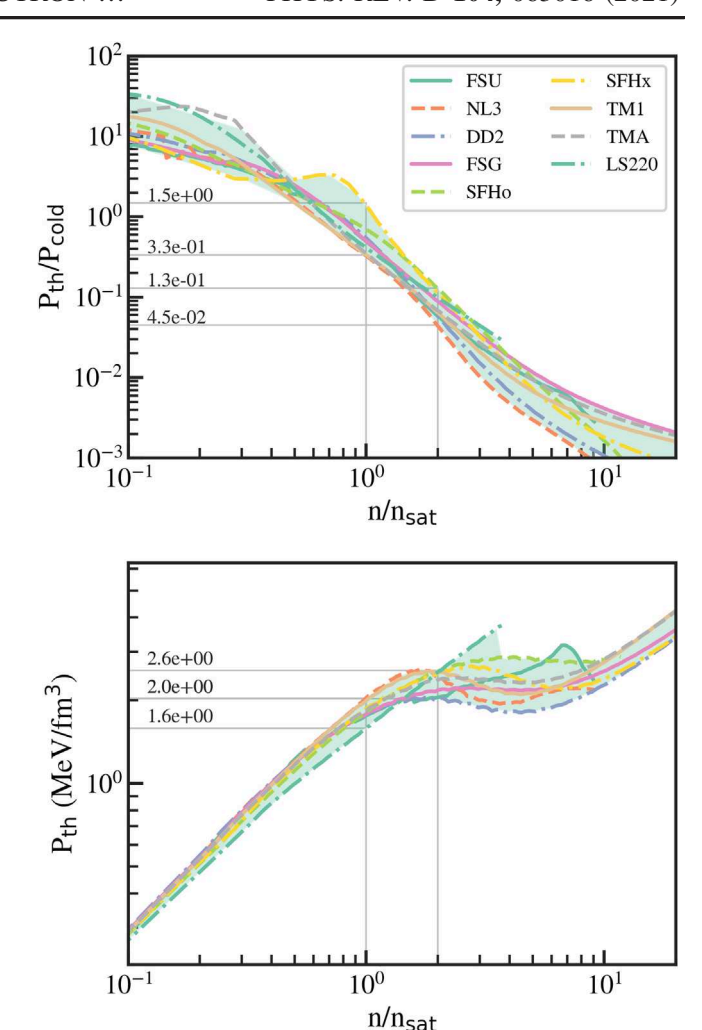


FIG. 1. Top: Ratio of thermal-to-cold pressure as a function of the density for various finite-temperature EoSs. Bottom: magnitude of the thermal pressure for the same EoSs. For each EoS, the thermal pressure is computed at $k_BT=20$ MeV and $P_{\rm cold}$ is at $k_BT=0.1$ MeV, for proton fraction of $Y_p=0.1$. The vertical lines correspond to the nuclear saturation density, $n_{\rm sat}=0.16~{\rm fm^{-3}}$, and $2n_{\rm sat}$, while the horizontal lines indicate the maximum range in the tabulated EoSs at these densities. The green shading is included to visually highlight the range in thermal pressures spanned by these EoSs.

tabulated EoSs, and is thermodynamically cold in that the temperature is much less than the Fermi energy of nucleons. The bottom panel of Fig. 1 shows the magnitude of the thermal pressure under the same conditions. For these EoSs, the thermal pressure can significantly exceed the cold pressure at low densities; $P_{\rm th}$ can be comparable to $P_{\rm cold}$ at the nuclear saturation density ($n_{\rm sat}=0.16~{\rm fm^{-3}}$); and $P_{\rm th}$ is still ~10% of the cold pressure at $2n_{\rm sat}$. Moreover, there is significant variation between the tabulated EoSs, with the ratio of $P_{\rm th}/P_{\rm cold}$ differing by a factor of 5 at $n_{\rm sat}$ and by a factor of 3 at $2n_{\rm sat}$, between these EoSs. We also note that the temperature after a binary neutron star merger can reach even higher values than those considered

Configuration Gravitational mass Initial temperature Cold EoS Thermal treatment $\Gamma_{th} = 1.66$ $1.4~M_{\odot}$ $P_{\rm th} = 0$ Single star $\Gamma = 2$ polytrope $M^*(n_0 = 0.12 \text{ fm}^{-3}, \alpha = 0.8)$ $P_{\rm th} = 0.1 P_{\rm cold}$ Single star $1.4~M_{\odot}$ $\Gamma = 2$ polytrope $\Gamma_{th} = 1.66$ $M^*(n_0 = 0.12 \text{ fm}^{-3}, \alpha = 0.8)$ $1.4 \ M_{\odot} + 1.4 \ M_{\odot}$ $P_{\rm th} = 0$ **NSNS** ENG (piecewise polytropes) $\Gamma_{\text{th}} = 1.5$ $M^*(n_0 = 0.08 \text{ fm}^{-3}, \alpha = 0.6)$ $M^*(n_0 = 0.08 \text{ fm}^{-3}, \alpha = 1.3)$ $M^*(n_0 = 0.22 \text{ fm}^{-3}, \alpha = 0.6)$ $M^*(n_0 = 0.22 \text{ fm}^{-3}, \alpha = 1.3)$

TABLE I. Summary of tests run. The parameters n_0 and α in the M^* model are described below.

here, with temperatures up to 40–50 MeV at 2– $3n_{\rm sat}$, in which case the thermal pressure can be up to $\sim 50\%$ of the cold pressure at supranuclear densities, as we show in Sec. V B.

Thus, even within the family of commonly-used EoS tables, thermal effects remain quite uncertain. This uncertainty may be reduced through observations of neutron stars at high temperatures, such as during the late stages of a binary neutron star merger. However, constraining the finite-temperature part of the EoS requires one to be able to untangle the role of the cold EoS, which is uncertain in its own right, from any thermal effects. This is not straightforward in simulations adopting tabulated finitetemperature EoSs, e.g., [12,41-46]. However, the analytic framework of the M^* -approximation, with its physicallymotivated parameters that can be varied systematically and independently of the cold EoS, provides one major step forward toward the goal of constraining the finite-temperature EoS with future observations of NSNS mergers. We begin to explore this approach in this work.

III. OVERVIEW OF SIMULATIONS PERFORMED

In this paper, we implement the M^* -approximation into NSNS merger simulations in full numerical relativity. In order to validate the implementation and performance of the M^* -EoS, we run three different types of tests. For each test, we evolve the initial data with:

- (1) the hybrid approximation with a constant Γ_{th} , and
- (2) the M^* -approximation,

each added to the same cold EoS.

In the first set of tests, we evolve a single rotating, cold neutron star, in order to ensure that the star remains cold over time. In the second, we evolve a rotating, single neutron star, to which we add a nonzero temperature gradient. By studying whether the temperature gradient can be maintained without loss of stability and without spurious growth, this provides a more stringent test of the M^* -EoS. Finally, we evolve a set of NSNS mergers with a large range of M^* -parameters. This enables us to study the performance of the M^* -EoS in a dynamical setting, in which the stars start cold and develop significant temperature gradients through shock-heating. Additionally, by using a wide range of M^* -parameters, we perform an initial parameter study of how each M^* -parameter affects the latestage properties of an NSNS merger and we compare the outcomes to the ideal-fluid approximation. We summarize the various tests run in Table I.

IV. NUMERICAL METHODS

All simulations were performed with the Illinois dynamical spacetime, general-relativistic magnetohydrodynamics (GRMHD), adaptive-mesh-refinement code, which has most recently been described in Etienne *et al.* [47], and is built within the Cactus/Carpet framework [48–50]. The spacetime is evolved using the Baumgarte-Shapiro-Shibata-Nakamura formulation of the Einstein equations [51,52]. We use 1 + log time slicing of the lapse [53] and a 2nd-order "Gamma-driver" condition for the shift [54]. Additionally, we modified the original Illinois GRMHD code to use the primitive variable recovery routine described in East *et al.* [55].

A. The M^* -approximation of thermal effects

During the evolutions, the EoS is calculated locally at each time step. The total energy and pressure are taken to be the sum of a cold component and a thermal component, as in Eqs. (1a)–(1b). For the hybrid evolutions, the thermal component is trivially calculated according to Eq. (2), for constant $\Gamma_{\rm th}$. In the M^* -formalism, the thermal pressure and energy are not so simply related. In this section, we summarize the M^* -framework for calculating $P_{\rm th}$ and $E_{\rm th}$ from one another, as was first presented in RÖP.

In this framework, the thermal energy per baryon and the thermal pressure are given by

$$E_{\text{th}}(n, T, Y_p) = \frac{4\sigma f_s T^4}{cn} + \left\{ \left(\frac{3k_B T}{2} \right)^{-1} + \left[a(n, Y_p = 0.5, M_{\text{SM}}^*) + a(n, Y_p, m_e) Y_p \right]^{-1} T^{-2} \right\}^{-1}$$
(3a)

$$P_{\rm th}(n,T,Y_p) = \frac{4\sigma f_s T^4}{3c} + \left\{ (nk_B T)^{-1} - \left[\frac{\partial a(n,Y_p = 0.5,M_{\rm SM}^*)}{\partial n} + \frac{\partial a(n,Y_p,m_e)}{\partial n} Y_p \right]^{-1} n^{-2} T^{-2} \right\}^{-1} \tag{3b}$$

where n is the baryon number density, T is the temperature, Y_p is the proton fraction, σ is the Stefan-Boltzmann constant, c is the speed of light, f_s is the number of relativistic species, a is the level-density parameter, $M_{\rm SM}^*$ is the relativistic Dirac effective mass of symmetric nuclear matter, and m_e is the electron mass. The adiabatic sound speed can also be calculated within this framework, as in Appendix B of RÖP. We note that in the original framework of RÖP, there was a typo, such that $M_{\rm SM}^*$ was incorrectly preceded by a factor of 0.5 in the level-density parameter term. We have corrected this expression in Eqs. (3a) and (3b) and in the remainder of the present work (see [56] for further details).

Equations (3a) and (3b) each consist of three terms, which characterize the different density regimes that can be encountered in an NSNS merger. The first term ($\propto T^4$) describes the energy of a relativistic gas of particles with f_s degrees of freedom. This term dominates at very low densities and thus will affect the atmosphere and lowdensity outflows during a merger. The second term ($\propto T$) is the ideal fluid contribution, which dominates at intermediate densities, up to $\sim n_{\rm sat} = 0.16 \text{ fm}^{-3}$. At higher densities $(\gtrsim n_{\rm sat};$ although the exact transition density depends sensitively on the temperature), the matter is degenerate and the corresponding thermal energy scales as T^2 at leading-order. Adding the ideal and degenerate-limit terms inversely ensures that the degenerate term dominates at high densities and guarantees a smooth transition between the ideal and degenerate regimes. We note, however, that doing this separately in Eqs. (3a) and (3b) means that these quantities are no longer exactly thermodynamically linked across the narrow range of densities where the transition occurs (for further discussion, see RÖP).

When calculating the number of relativistic species that contribute to the thermal energy, we consider two limits. For $k_bT \ll 2m_ec^2$, photons are the dominant relativistic species, making $f_s=1$. For $k_BT\gg 2m_ec^2$, electrons and positrons become relativistic as well, each with 7/8 degrees of freedom, and thus $f_s=11/4$. At temperatures above 10 MeV, thermal neutrinos and anti-neutrinos appear; however, following the convention of common finite-temperature EoS tables, we neglect the thermal contribution from neutrinos in this calculation, but it is straightforward to account for them in our approach. In order to smoothly connect the two temperature regimes of interest, we approximate the number of relativistic species with a simple linear interpolation, according to

$$f_S = \begin{cases} 1, & k_B T < 0.5 \text{ MeV}, \\ -0.75 + 3.5 \left(\frac{k_B T}{1 \text{ MeV}}\right), & 0.5 \le k_B T < 1 \text{ MeV}, \\ 11/4, & k_B T \ge 1 \text{ MeV}. \end{cases}$$
 (4)

At higher densities, the degenerate thermal terms are characterized by the level-density parameter,

$$a(n,Y_p,M_q^*) \equiv \frac{\pi^2 k_B^2}{2} \frac{\sqrt{(3\pi^2 Y_p n)^{2/3} (\hbar c)^2 + M_q^{*2}}}{(3\pi^2 Y_p n)^{2/3} (\hbar c)^2}, \quad (5)$$

where n_q and M_q^* are the density and relativistic Dirac effective mass of the species, respectively. Here, we consider only symmetric nuclear matter, for which the relevant species are protons, neutrons, and electrons, and we neglect the small change to the thermal pressure caused by the matter having unequal numbers of protons and neutrons (see RÖP for additional details). In symmetric matter, the number densities of protons and neutrons are equal by definition (i.e., $n_p = n_n = 0.5n$), and we take the neutron and proton effective masses to be comparable as well, such that $M_p^* \approx M_n^* \approx M_{\rm SM}^*$, where the last term is the symmetric matter effective mass. We parametrize the effective mass function as

$$M_{\rm SM}^* = \left\{ (mc^2)^{-2} + \left[mc^2 \left(\frac{n}{n_0} \right)^{-\alpha} \right]^{-2} \right\}^{-1/2}, \quad (6)$$

where n is the total baryon number density.

In this parametrization, we fix the low-density baryon mass to the energy per baryon of 56 Fe, $mc^2 = 930.6$ MeV. This leaves us with two free parameters: n_0 , which controls the density at which degeneracy becomes significant, and α , which controls the rate at which the effective mass decreases at high densities and which is related to the strength of the particle interactions in the matter. These are the parameters that will be varied in our NSNS evolutions. The effective mass of the electrons is approximately constant due to their small interaction cross section, so their effective mass simply reduces to the electron mass.

For the bulk of the matter within a neutron star merger remnant, the neutrino opacity is expected to be large enough that the neutrinos are trapped on the timescales considered in this paper [13,57]. As a result, the local proton fraction in the remnant is not changed by neutrino

interactions, although Y_p can deviate from its initial β -equilibrated value through advection. Because Y_p does not enter the hybrid approximation of Eqs. (1a)–(1b), it is not possible to consider the advection of Y_p within that framework. Thus, in the regime of large neutrino opacities, the hybrid approximation implicitly requires that the matter remains in its initial composition (i.e., cold β -equilibrium), so that the cold pressure expression does not change. In order to perform the most direct comparison between the M^* - and the hybrid approximation, in this work we also assume that the matter maintains its initial cold, β -equilibrium composition. It should be noted, however, that the most general form of the M^* -formalism allows for full composition dependence [24].

Accordingly, we set the proton fraction of the matter at each time step such that it corresponds to that of cold β -equilibrium. For nucleonic matter in β -equilibrium, the proton fraction is uniquely given by the local density and the symmetry energy, E_{sym} , according to

$$Y_{p,\beta}(n) = \frac{1}{2} + \frac{(2\pi^2)^{1/3}}{32} \frac{n}{\xi} \times \left\{ (2\pi^2)^{1/3} - \frac{\xi^2}{n} \left[\frac{\hbar c}{E_{\text{sym}}(n, T = 0)} \right]^3 \right\}, \quad (7)$$

where, for simplicity, we have introduced the auxiliary quantity ξ , defined as

$$\xi \equiv \left[\frac{E_{\text{sym}}(n, T = 0)}{\hbar c} \right]^{2} \times \left\{ 24n \left[1 + \sqrt{1 + \frac{\pi^{2}n}{288} \left(\frac{\hbar c}{E_{\text{sym}}(n, T = 0)} \right)^{3}} \right] \right\}^{1/3}.$$
(8)

We parametrize the nuclear symmetry energy in terms of a kinetic and potential-like term [as in [58,59]], according to

$$E_{\text{sym}}(n, T = 0) = \eta E_{\text{sym}}^{\text{kin}}(n) + \left[S_0 - \eta E_{\text{sym}}^{\text{kin}}(n_{\text{sat}})\right] \left(\frac{n}{n_{\text{sat}}}\right)^{\gamma},$$
(9)

where S_0 is the value of the symmetry energy at the nuclear saturation density. The "kinetic" term, $E_{\rm sym}^{\rm kin}$ arises from the change in the Fermi energy, E_F , of a gas as the relative densities of protons and neutrons $(n_n \text{ and } n_p)$ change, and is given by 1

$$E_{\text{sym}}^{\text{kin}}(n) = \frac{3}{5} \left[E_F \left(n_p = n_n = \frac{1}{2} n \right) - E_F(n_n = n) \right]$$
 (10)

where

$$E_F(n_q) = \frac{\hbar^2}{2m} (3\pi^2 n_q)^{2/3}.$$
 (11)

The potential-like term in Eq. (9) is less well understood and is, thus, given an arbitrary density-dependence above the nuclear saturation density, n_{sat} , through the free parameter γ . Finally, the parameter η , which accounts for the short-range correlations [60–65], can be written as

$$\eta = \frac{5}{9} \left[\frac{L_0 - 3S_0 \gamma}{(2^{-2/3} - 1)(2/3 - \gamma)E_F(n_{\text{sat}})} \right], \tag{12}$$

where L_0 is related to the slope of E_{sym} at n_{sat} .

We adopt the full symmetry energy model described above for the regime of uniform, nuclear matter, i.e., at densities above $0.5n_{\rm sat}$. At lower densities, however, this model breaks down. Thus, for $n < 0.5n_{\rm sat}$, we transition to a function that smoothly decays to zero, such that the symmetry energy is given by

$$E_{\text{sym}}(n) = E_{\text{sym}}(0.5n_{\text{sat}}) + P_{\text{sym}}(0.5n_{\text{sat}}) \left[\frac{\left(\frac{n}{0.5n_{\text{sat}}}\right)^{x-1} - 1}{0.5n_{\text{sat}}(x-1)} \right],$$

$$n < 0.5n_{\text{sat}}$$
(13)

where x is empirically determined to ensure that $Y_{p,\beta}$ rises to 0.5 at low densities, and where $P_{\rm sym}(n) \equiv n^2 \partial E_{\rm sym}/\partial n$ (see [24] for the full expression). The form of this low-density symmetry energy is chosen to ensure a reasonable behavior of $Y_{p,\beta}$ at low densities.

In this work, we fix the symmetry energy parameters to values that best fit the SFHo finite-temperature EoS, with $S_0 = 31.57$ MeV, $L_0 = 47.10$ MeV, and $\gamma = 0.41$ [24,66]. The SFHo EoS is based on a relativistic mean field theory calculation, using the statistical model of Hempel and Schaffner-Bielich [18], and is constructed to be consistent both with experimental nuclear data and astrophysical observations of neutron stars; additionally, SFHo has similar cold neutron star properties to ENG, which is the cold EoS used in our binary neutron star merger calculations (see Sec. IV B).

Finally, we need to be able to convert between the energy and the total pressure. Unlike in the hybrid approximation of Eq. (2), Eqs. (3a) and (3b) describe multiple regimes, each of which have a different density- and temperature-dependence. As a result, there is no simple expression for $P_{\rm th}$ in terms of $E_{\rm th}$ and vice versa. We can, nevertheless, simply convert between these quantities as follows: Given the density, $Y_{p,\beta}(n)$, and one thermodynamic quantity—either $E_{\rm th}$ or $P_{\rm th}$ —we use Eq. (3a) or (3b) to numerically

 $^{^{1}}$ We note that there was a factor-of-2 typo in the equation for $E_{\text{sym}}^{\text{kin}}$ in RÖP which has been corrected in Eqs. (10) and (12).

solve for the temperature, using a combination of the Newton-Raphson and bisection methods. We then use n, $Y_{p,\beta}(n)$, and the inverted temperature to directly calculate the other thermodynamic variable.

When implementing this framework numerically, we also need to adopt one additional modification. During binary neutron star evolutions, numerical errors can cause the total pressure to drop below the cold pressure. By Eq. (1b), this would imply the thermal pressure has become negative; but, negative thermal pressures are not allowed within the microphysical M^* -framework. To mitigate this unphysical error, we impose a pressure floor to prevent the thermal pressure from becoming too negative. It was previously shown in [47] that setting the pressure floor at exactly P_{cold} can cause large drifts in the central density of single-star evolutions; as a result, we adopt an intermediate pressure floor of $0.9P_{\text{cold}}$. In the regime where the thermal pressure or energy become negative, we switch to a hybrid EoS with $\Gamma_{th}=2$ in order to facilitate the conversion between $E_{\rm th}$ and $P_{\rm th}$.

Because the M^* -framework involves only two free parameters (n_0 and α ; as we are fixing the symmetry energy parameters), we find that implementing the M^* -framework into binary evolution calculations introduces a slowdown of only $\sim 30\%$ to the overall speed of the code, compared to an identical evolution with the hybrid approximation.

1. M*-parameters explored in this work

For a sample of nine finite-temperature EoS tables, the M^* -parameters have been found to range between $n_0 \in [0.10-0.22] \text{ fm}^{-3}$ and $\alpha \in [0.72-1.08]$, for symmetric nuclear matter [24]. For our single star tests, we use one representative set of parameters, with $n_0 = 0.12 \text{ fm}^{-3}$ and $\alpha = 0.8$. For the binary evolutions, we explore values of

 $n_0 = 0.08$ and 0.22 fm⁻³, and $\alpha = 0.6$ and 1.3, which approximately bracket the range found in the sample of tabulated EoSs cited above. These choices of parameters are summarized in Table I.

An effective thermal index for each of these models can be calculated according to

$$\Gamma_{\text{th}} = 1 + \left(\frac{P_{\text{th}}(n, T, Y_p)}{nE_{\text{th}}(n, T, Y_p)}\right). \tag{14}$$

The resulting thermal indices for the five parameter combinations used in this work are shown in Fig. 2. We also include in Fig. 2 the thermal index for several finitetemperature EoS tables, as dotted lines, for comparison. We find a strong density dependence in the thermal index for all of the M^* EoSs, as expected. The range of Γ_{th} for the four extremal M^* -parameters approximately brackets the range of tabulated Γ_{th} , as intended. The set of M^* -parameters used for the single-star test ($n_0 = 0.12 \text{ fm}^{-3}$, $\alpha = 0.8$; shown in gray in Fig. 2) was chosen as a more realistic set of parameters, and it can be seen in Fig. 2 that this choice is approximately consistent with the equivalent Γ_{th} of the tabulated EoSs considered. Figure 2 also demonstrates the dependence of Γ_{th} on the M^* -parameters: namely, we find that the density at which Γ_{th} starts to vary is directly governed by the parameter n_0 , while the degree of density-dependence is determined by the parameter α . Microphysically, we can interpret n_0 as being related to the density at which particle interactions start to become significant and α as corresponding to the strength of those particle interactions.

Finally, we note that for these M^* -parameters and for the regimes probed in our binary evolutions ($n \lesssim 5n_{\text{sat}}$; see Sec. VB), the sound speed predicted by the complete EoS is always subluminal.

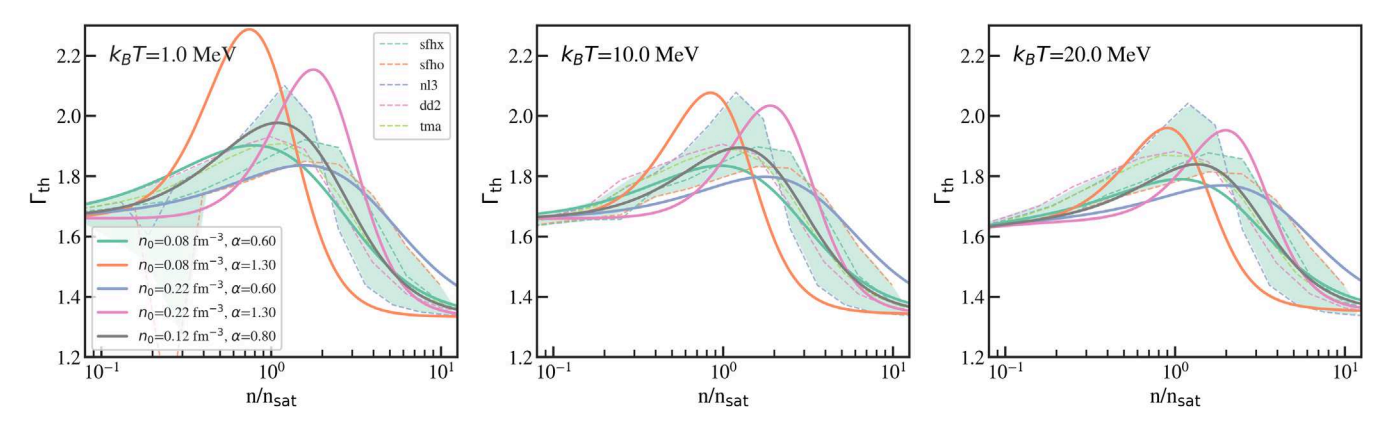


FIG. 2. Effective thermal index for the parameters explored in this work at three different temperatures. From left to right, the panels show $\Gamma_{\rm th}$ at $k_BT=1$, 10, and 20 MeV; all panels are calculated for matter in neutrino-less β -equilibrium. We also show the effective thermal index for a sample of finite-temperature EoSs as dotted lines, for comparison. The green shading is included to visually represent the range of $\Gamma_{\rm th}$ values spanned by the realistic EoS tables. All sets of M^* -parameters confirm that $\Gamma_{\rm th}$ indeed depends on the density. The degree of density-dependence is directly governed by the parameter α , while the density at which $\Gamma_{\rm th}$ begins to vary is determined by the parameter n_0 .

B. Initial conditions

We now describe the initial conditions for the various tests performed in this paper. The single-star initial data were constructed using the code of Cook et al. [67,68]. For both temperature configurations, we used a $\Gamma = 2$ polytrope for the cold EoS and we assumed the matter was initially in β -equilibrium, with the proton fraction set according to Eq. (7). For the zero-temperature test, this completely describes the EoS. For the finite-temperature single-star test, we added a thermal gradient to this cold EoS, such that the thermal pressure is 10% of the cold pressure at all densities. We constructed one EoS table with the $P_{\rm th}/P_{\rm cold}=0.1$ profile assuming $\Gamma_{\rm th}=1.66$ to calculate the associated energies, as well as a second EoS table with the same thermal pressure profile but instead assuming the M^* -approximation with $n_0 = 0.12 \text{ fm}^{-3}$ and $\alpha = 0.8$. For all single-star tests, the gravitational mass of the stars was 1.4 M_{\odot} and the stars were set to be rapidly rotating, such that the ratio of rotational to gravitational binding energy was T/W = 0.037, with a ratio of the polar-toequatorial radii of 0.85. We note that while the ratio T/W is the same for the three tests considered here, the individual values of T and W vary between them.

The binary neutron star initial data were constructed with the Compact Object Calculator (COCAL) code [69–71]. The initial configuration describes two unmagnetized, equalmass neutron stars in a quasicircular orbit, with an Arnowitt-Deser-Misner (ADM) mass of 2.8 M_{\odot} , an initial separation of 35 km, and ADM angular momentum of $J_{\rm ADM}/M_{\rm ADM}^2 = 0.93$. The neutron stars start at zerotemperature and are described by a piecewise polytropic representation of the ENG EoS ([72,73], as fit for in [74]). With this EoS, the radius of a 1.4 M_{\odot} , nonspinning, cold neutron star is 12.06 km and the corresponding maximum mass is $2.24 M_{\odot}$. Both properties are consistent with the latest astrophysical observations (for a review of neutron star radii, see e.g., [15]; for maximum mass constraints, [75–78]). For the rotating configuration used here, the coordinate equatorial radii of the initial stars is 9.2 km.

C. Grid hierarchy

For the single star evolutions, we use a fixed mesh refinement grid hierarchy, consisting of 7 refinement levels, each with a 2:1 refinement ratio. The half-side length of the finest level is set to be 30% larger than the coordinate equatorial radius of the neutron star, so that the entire star is contained within the innermost refinement level. This level has grid spacing such that the equatorial diameter of the neutron star is covered with 82 points for the baseline resolution. We also run high-resolution evolutions with half this grid spacing (i.e., 164 grid points across the star).

For the binary evolutions, we use 9 refinement levels, again each with a 2:1 refinement ratio. The computational domain extends across $[-3025, 3025]^2 \times [0, 3025]$ km.

Equatorial symmetry is imposed to save computational resources. The baseline resolution corresponds to ~ 100 points across the diameter of each initial neutron star at the finest level, with a resolution of $dx_{\rm finest} \approx 0.18$ km. We also perform simulations at $1.5625\times$ and $2\times$ the baseline resolution for the M^* -EoS with $n_0=0.08$ fm⁻³ and $\alpha=1.3$ (i.e., using ~ 150 and 200 points across the diameter of each initial star, respectively).

D. Diagnostics

We use several diagnostic quantities to analyze the simulation output. For all evolutions, we monitor the L2 norm of the Hamiltonian constraint, $\|\mathcal{H}\|$, in order to validate our numerical calculations. We also track the evolution of the maximum rest-mass density in order monitor the stability of the stars against gravitational collapse.

Additionally, we extract gravitational radiation using the Newman-Penrose Weyl scalar ψ_4 , which is related to the GW strain via $\psi_4 = \ddot{h}_+ - i \ddot{h}_\times$. The Weyl scalar is decomposed on spheres at large radii $(r \ge 120M)$ into s = -2 spin-weighted spherical harmonics, such that

$$\psi_4(t, r, \theta, \phi) = \sum_{\ell=2}^{\infty} \sum_{m=-\ell}^{\ell} \psi_4^{\ell m}(t, r)_{-2} Y_{\ell m}(\theta, \phi)$$
 (15)

where θ and ϕ are defined with respect to angular momentum axis, r is the extraction radius, and t is the time. The total strain, $h \equiv h_+ - ih_\times$, is then given by

$$h(t,r,\theta,\phi) = \int_{-\infty}^{t} dt' \int_{-\infty}^{t'} dt'' \psi_4(t'',r,\theta,\phi). \quad (16)$$

We calculate the double time integration using the fixed-frequency integration (FFI) method [79].

Finally, we calculate the amount of matter ejected during the NSNS evolutions by integrating the total rest-mass density, ρ_b , outside of a given radius r and for matter for which $-u_t > 1$, according to

$$M_{\rm ej}(>r) = \int_{\sim r} \rho_b u^t \sqrt{-g} d^3x, \qquad (17)$$

where u^t is the time-component of the fluid 4-velocity and g is the determinant of the metric.

V. SIMULATION RESULTS

We now turn to the results of our numerical simulations. We start with a brief summary of the findings from the single star evolutions (for further details, see Appendix B). We find that rotating stars evolved with the M^* -EoS indeed maintain their initial temperature profile and remain stable, for both cold and finite-temperature initial data. Additionally, both M^* evolutions exhibit second-order convergence in the central rest-mass density over time, as expected from our

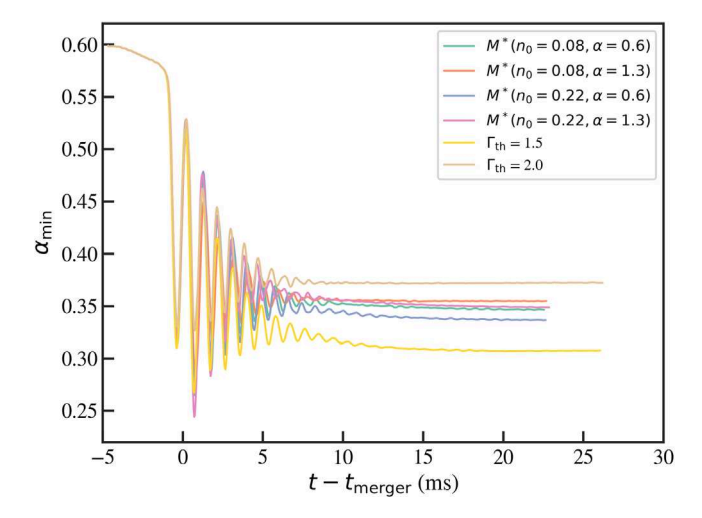


FIG. 3. Minimum lapse, α_{min} , as a function of time since merger, for the six thermal treatments considered in this paper. The minimum lapse is approximately constant at late times, indicating that the remnant remains stable against collapse until the end of our simulations.

numerical scheme. With this validation of our numerical methods now in hand, we devote the remainder of this section to the results of the binary star evolutions.

A. Stability and convergence

For all the M^* -parameter choices and for both constant Γ_{th} evolutions, we find that the neutron stars remain stable and show no signs of significant heating prior to merger, as is consistent with previous findings [e.g., [8]]. As a result, all thermal treatments lead to nearly identical inspirals.

The rest mass of the merger remnant is $\sim 3.23~M_{\odot}$, which exceeds the maximum rest mass for the zero-temperature Kepler sequence of $3.17~M_{\odot}$. This suggests that the remnant is likely supported by differential rotation, with the thermal pressure providing additional support [13], but that the remnant should eventually collapse. However, we find no signs of collapse by the end of our evolutions, which last for ~ 20 ms following the merger for the M^* -EoSs and 25 ms postmerger for the hybrid evolutions. Figure 3 shows that the minimum lapse function remains stable at late times, indicating that the remnant has not started collapsing by the end of these simulations, for all thermal treatments considered here.

Finally, we also perform evolutions at 1.5625 and $2\times$ the baseline resolution for the EoS with M^* -parameters $n_0 = 0.08 \text{ fm}^{-3}$ and $\alpha = 1.3$. We find second-order convergence of $\|\mathcal{H}\|$ during the inspiral and for the first few milliseconds postmerger, which then decays at later times (see Appendix C for more details).

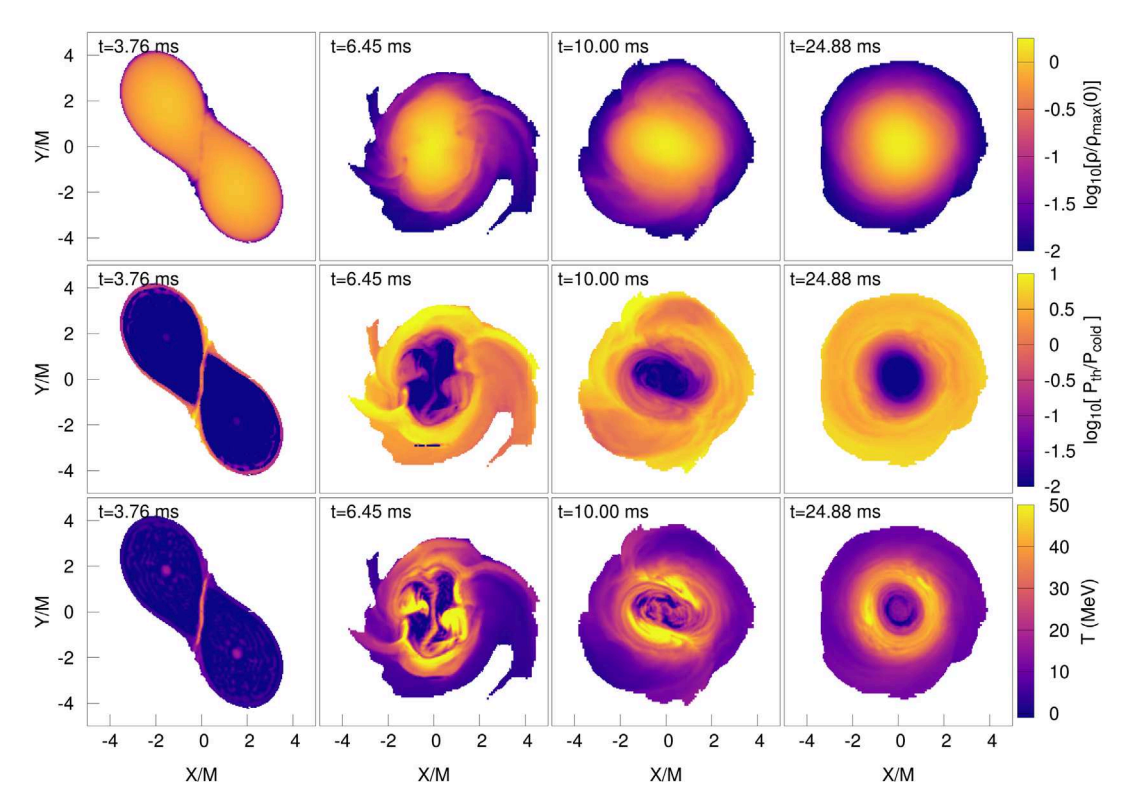


FIG. 4. Top: density profile just before and at three snapshots after merger, for the M^* -EoS with $n_0=0.08~{\rm fm^{-3}}$ and $\alpha=1.3$. Middle: thermal pressure profile, relative to the cold pressure, at the same times. Bottom: temperature profile, extracted from the density and thermal pressure using the microphysical model of Eq. (3b). All plots only include matter with densities above $0.01\times$ the initial maximum rest-mass density, $\rho_{\rm max}(0)$.

B. Post-merger evolution

In order to give a qualitative sense of the behavior of the density and thermal profiles over time, we show 2D snapshots from the M^* -EoS simulation with $n_0 = 0.08$ fm⁻³ and $\alpha = 1.3$ in Fig. 4, just prior to merger and at select times postmerger. The top row shows 2D rest-mass density profiles; the middle row shows the thermal pressure relative to the cold pressure; and the bottom row shows the corresponding temperature, which is computed from Eq. (3b). For comparison, we also show the late-time (t = 24.88 ms) 2D profiles for all four M^* -EoSs in Fig. 5, with different M^* -parameters shown in each column. In each of these figures, we only include matter with densities above 10^{-2} × the initial central density of each star, $\rho_{\rm max}(0)$, with lower-density material masked in white. Additionally, in Figs. 4 and 5, wherever the thermal pressure is negative, it is replaced with zero for display purposes (i.e., both zero and negative thermal pressures are shown as dark purple, to indicate the matter is "cold"; see Sec. IVA for further discussion).

From the snapshots shown in Figs. 4 and 5, several trends emerge. First, we find evidence of significant heating at supranuclear densities. Figure 4 shows that the stars remain cold prior to merger, but that the thermal pressure can reach a few tens of percent of the cold pressure shortly following merger. At late times, Fig. 5 shows that

differences persist in the thermal pressure profile depending on the M^* -parameters, with higher $P_{\rm th}/P_{\rm cold}$ in the outer layers of the remnant for evolutions with $n_0=0.22~{\rm fm}^{-3}$ than with $n_0=0.08~{\rm fm}^{-3}$. However, for all M^* parameters, the very core of the star (e.g., $|X/M|\lesssim 1$) remains thermodynamically cold ($P_{\rm th}\lesssim 0.1P_{\rm cold}$) at late times.

Additionally, in comparing these snapshots, it becomes clear that small differences in the thermal pressure can translate to large differences in the temperature profile of the remnant, due to the $\propto T^2$ dependence in Eq. (3b), which dominates at high densities. From the bottom panel of Fig. 5, we find that larger values of α correspond to higher core temperatures at late times. When α is large, M^* decays more quickly. Thus, Fig. 5 suggests that having a small effective mass at the core leads to larger core temperatures. This is similar to the findings from 1D CCSN simulations, in which EoSs with a smaller effective mass were found to produce larger central temperatures in the proto-neutron star [80,81]. However, we note that the trend breaks down at other densities in our merger remnants: that is, it is not generically true that temperature scales with the local effective mass at every density.

These findings suggest that the parameters of the M^* -approximation play a role in determining the postmerger thermal profile, with larger n_0 contributing to a higher degree of heating in the outer layers, and larger α

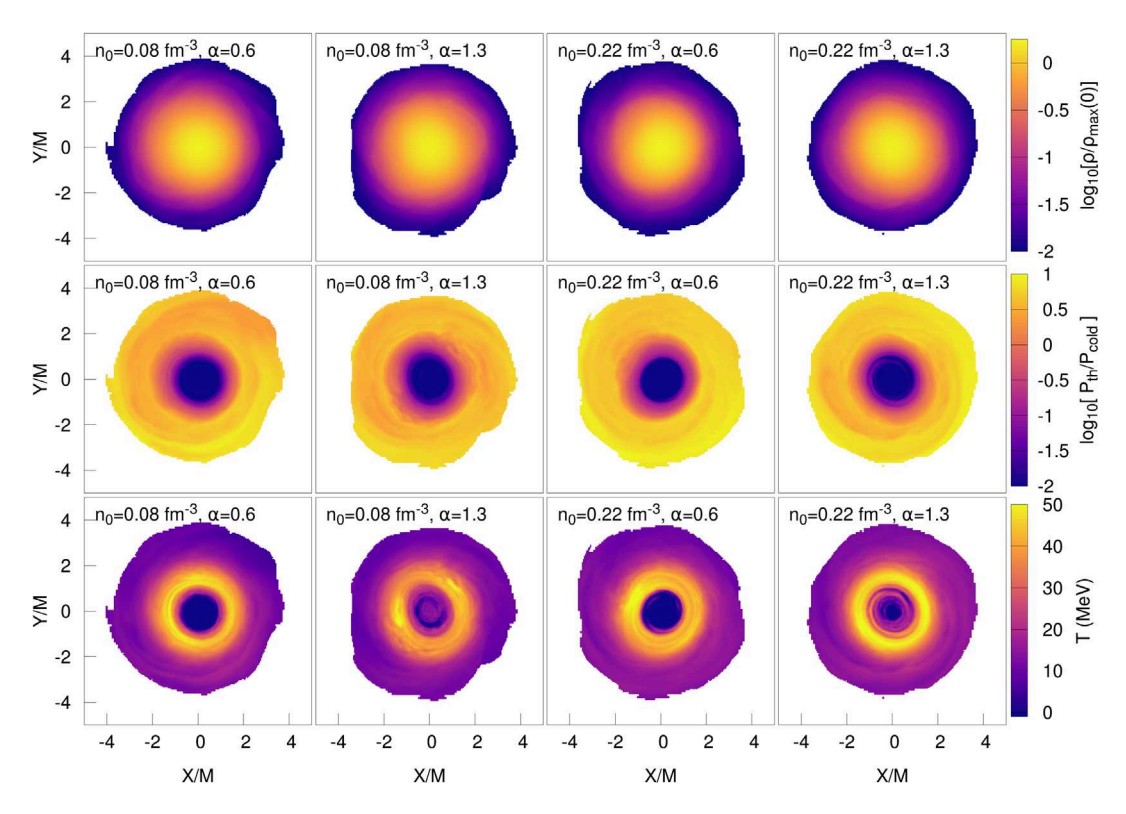


FIG. 5. Late-time (t = 24.88 ms) profiles for each of the M^* -EoSs. Each column corresponds to the specific set of M^* -EoSs parameters indicated, and the rows show the density (top), thermal pressure (middle), and temperature (bottom) profiles. We find that the thermal pressure in the outer layers of the star is primarily determined by the value of n_0 , while the temperature of the inner core ($|X/M| \lesssim 1$) is determined by α .

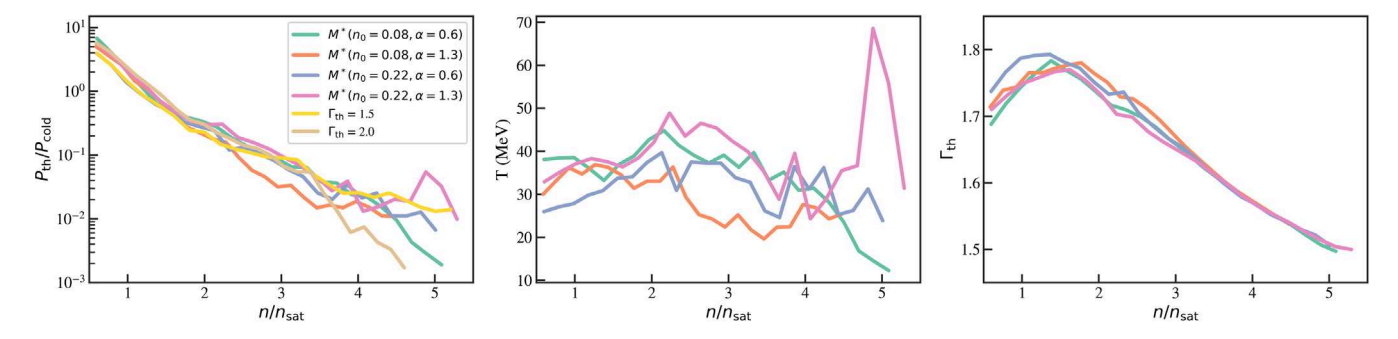


FIG. 6. Characteristic $P_{\rm th}/P_{\rm cold}$ (left), temperature (middle), and thermal index (right) at each density. We define the characteristic quantity as the median of the distribution of values within a particular density bin, at a fixed time just after merger ($t=6.5~{\rm ms}$). We only extract temperatures for the M^* -EoSs, which have a microphysical relationship between $P_{\rm th}$ and T.

contributing to hotter cores. As a result, the local neutrino emissivity, and hence the cooling and ultimate neutrino irradiation of the remnant disk likely will also depend on the parameters characterizing the finite temperature part of the EoS.

In order to be more quantitative in our comparison, we also calculate characteristic 1D profiles of the thermal pressure, temperature, and thermal index just after merger, when the matter has not yet been redistributed by the differing thermal pressures. To compute these characteristic quantities, we first bin all grid points along the equatorial plane at a fixed time (t = 6.5 ms), using density bins that are uniformly spaced between 0.5 n_{sat} and the core density. Within each density bin, we then compute the distribution of $P_{\rm th}/P_{\rm cold}$, T, and $\Gamma_{\rm th}$, and we take the median value as characteristic. We show these characteristic values as a function of the corresponding density bin in Fig. 6. We find that, at the nuclear saturation density, the thermal pressure can be a few times larger than the cold pressure, but that it decreases in relative importance at higher densities. At core densities ($\sim 5n_{\rm sat}$), the typical thermal pressure is $\lesssim 0.1P_{\rm cold}$ in all cases, but the exact value can vary by up to an order of magnitude at these densities, depending on the thermal treatment. The M^* evolution with $n_0=0.22~{\rm fm^{-3}}$ and $\alpha=$ 1.3 leads to the largest thermal pressure at the core just after merger, whereas the evolution with $n_0 = 0.08 \text{ fm}^{-3}$ and $\alpha = 0.6$ produces the coldest core. These thermal pressures correspond to core temperatures ranging from nearly 70 MeV to ~12 MeV, respectively. The other two sets of M^* parameters lead to nearly identical core temperatures. just after merger, but still differ significantly from each other M^* -EoS throughout the rest of the star.

The thermal pressure profile just after merger is particularly interesting to consider, since this governs in part the redistribution of matter within the remnant and, hence, the postmerger evolution. We show how the differences in $P_{\rm th}/P_{\rm cold}$ just after merger influence the resulting remnant structure in Fig. 7, where we plot 1D density profiles, extracted along the X-axis, at the end of our simulations ($t=24.88~{\rm ms}$). We find small differences in the central density of the remnant between our various evolutions, with

the M^* evolutions differing by $\lesssim 5\%$ and the hybrid evolutions differing by $\sim 15\%$ from one another. The late-time radial extent of the star differs more significantly depending on the thermal treatment, with large values of α or large Γ_{th} leading to a more extended mass distribution. Although coordinate size is not a gauge-invariant quantity, Fig. 7 is suggestive that differences in the thermal treatment may influence the final compactness of the remnant.

Finally, Fig. 8 shows the azimuthally averaged angular velocity, $\Omega = v^{\phi}$, as a function of the cylindrical coordinate radius, $\varpi = \sqrt{X^2 + Y^2}$, for each of the thermal treatments. These profiles are calculated on the equator of the remnant at the end of the evolution (t = 24.88 ms). We find that the angular velocity profile is sensitive to the finite-temperature part of the EoS, with core angular velocities that differ by up to 60% and peak angular velocities that differ by up to

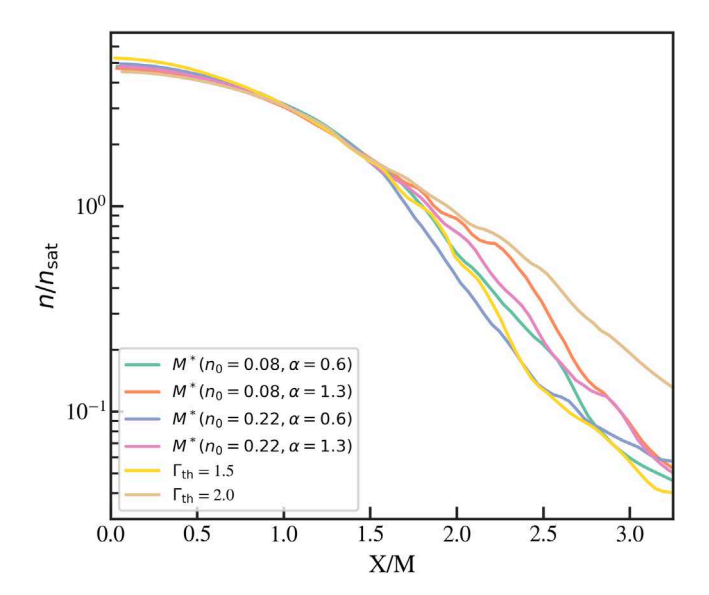


FIG. 7. Density profiles along the X-axis at late times (t = 24.88 ms), for the six different thermal treatments. Although the remnant starts with a similar density profile in all cases, the different thermal pressures in each of the six models cause the matter to be redistributed in noticeably different ways by late times.

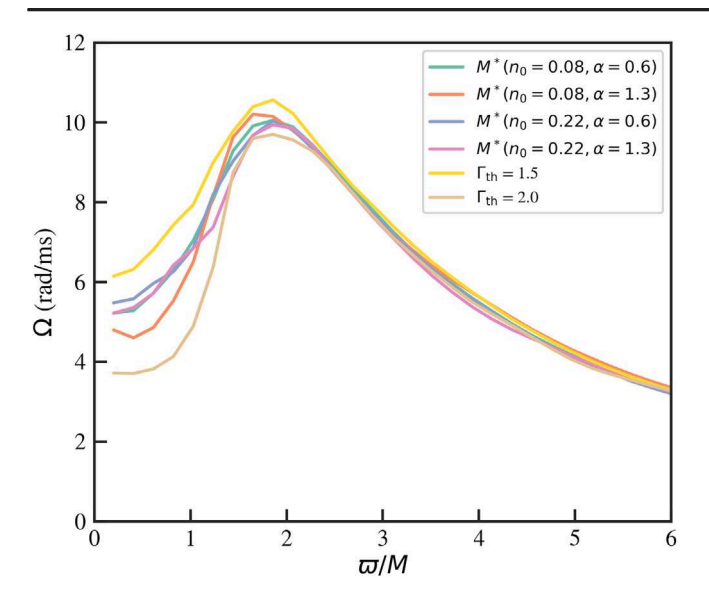


FIG. 8. Azimuthally averaged angular velocity profiles as a function of the cylindrical coordinate radius, on the equator of the remnant at late times ($t=24.88~\mathrm{ms}$). The different thermal treatments lead to up to 60% differences in the core angular velocities and 10% differences in the peak angular velocities, with a reduced range found between the M^* -parameters.

10% for the six thermal treatments explored here. Among only the M^* -EoSs, the range of angular velocities is smaller, with differences of up to ~14% and 3% in the core and peak angular velocities, respectively. Trends with particular M^* -parameters are harder to identify in these velocity profiles, but we note that the evolution with $n_0 = 0.08 \text{ fm}^{-3}$ and $\alpha = 1.3$ leads to the lowest core velocity and

the largest peak velocity. The other M^* -parameter choices lead to more similar velocity profiles. In all cases, the overall shape of the angular velocity profile remains the same as has been found in earlier studies (see [82] and discussion therein).

C. Gravitational wave signal

We extract the GW signal, as discussed in Sec. IV D, for each evolution and show the resulting strains in Fig. 9, for the $\ell=m=2$ mode. We separate the four M^* -EoS evolutions (left) from the two constant- $\Gamma_{\rm th}$ evolutions (right) for visual clarity. In all cases, the inspiral waveform is nearly identical, with a characteristic time to merger of 4.7 ms. By contrast, we find significant differences in the postmerger gravitational waves across all six thermal treatments. Figure 9 shows differences not only between the amplitudes of the postmerger strains, but also between the beat frequencies of the decaying signals, suggesting that the postmerger oscillation frequencies also depend on the thermal treatment.

Many previous studies have found evidence of empirical correlations between the oscillation frequencies of the postmerger GW signal and the neutron star radius or stellar compactness [for reviews, see [6,7,83]]. These correlations make it theoretically possible to constrain the properties of the initial, cold neutron stars through the measurement of the postmerger GW power spectrum. Using these types of relationships, it has been estimated that Advanced LIGO may constrain the radius to within 0.429 km for a nearby (≤30 Mpc) event [84]. It may be possible to get even smaller errors by coherently stacking postmerger spectra from multiple events with third-generation facilities, at which point systematic errors in the universal relations may

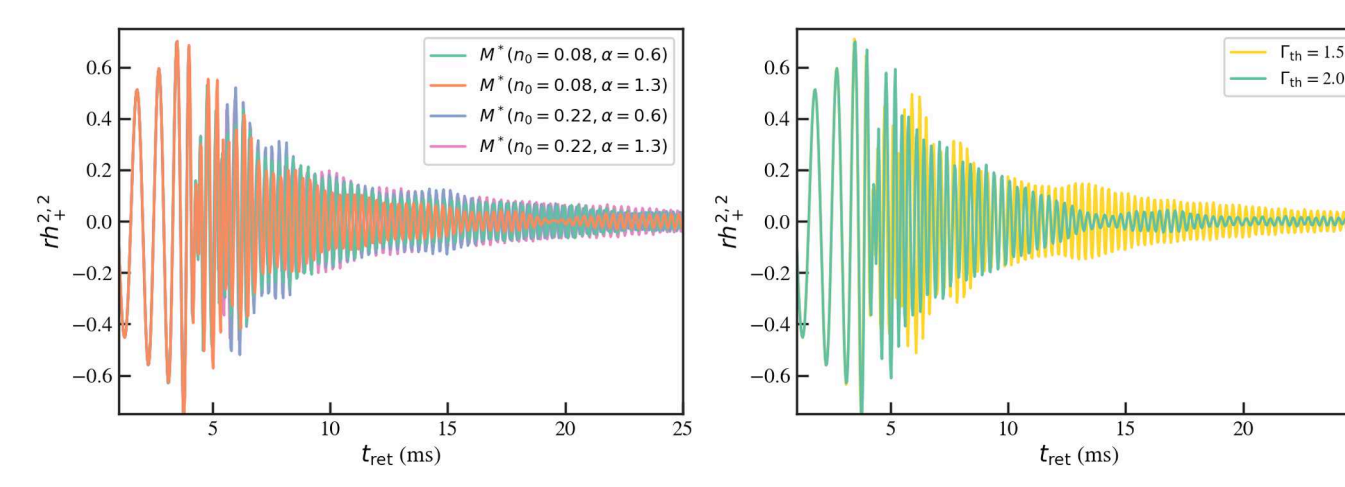


FIG. 9. Gravitational wave strain for the $\ell=m=2$ mode, for the six different evolutions, as a function of the retarded time. The gravitational wave signals from the M^* -EoS evolutions are shown in the left panel; the strains from the hybrid evolutions are shown in the right panel. In all cases, the inspiral phase is nearly identical, but we find significant differences in the postmerger gravitational waves.

dominate the error budget [85]. However, these estimates do not explicitly account for the uncertainties in the finite-temperature part of the EoS, which are hinted at in Fig. 9 and which may be important to take into account in order to extract precision radius estimates from such spectral features.

On the other hand, if the cold EoS can be pinned down from other observations—e.g., from the NSNS inspiral or from X-ray observations—then any remaining dependence of the postmerger oscillation frequencies on the M^* -parameters could potentially be used as an exciting new probe of the finite-temperature part of the nuclear EoS. We leave a more detailed exploration of the dependence of the postmerger GWs on the various M^* -parameters to future work.

D. Ejected mass

Finally, we also calculate the ejected mass for each of our evolutions via Eq. (17) for a sphere with radius 100M. Figure 10 shows the ejecta over time. We find a rapid rise in $M_{\rm ej}$ for the first ~10 ms postmerger. For the M^* -EoSs in particular, we find that the fastest $10^{-4}~M_{\odot}$ of ejecta have speeds of up to ~0.5 c for the M^* evolutions, while the fastest ejecta in the hybrid evolutions tend to be somewhat slower, with speeds of up to ~0.4 c.

We extract the amount of ejecta rest mass at the end of our simulations (20 ms postmerger). While $M_{\rm ej}$ is still slowly increasing at late times, due to the slow-moving tail of the distribution of ejecta, we use this value to facilitate an approximate comparison of $M_{\rm ej}$ between the different thermal treatments. We also note that the integration to compute $M_{\rm ej}$ introduces some error, which we estimate by comparing the extracted values of $M_{\rm ej}$ between a low- and high-resolution evolution. Based on this comparison, we

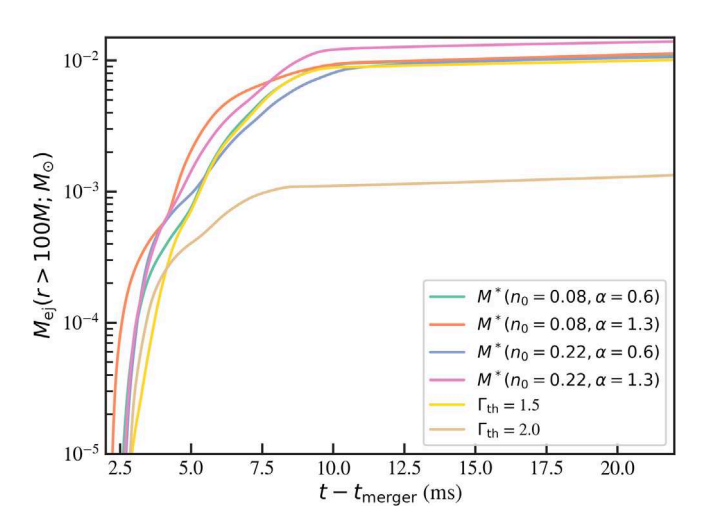


FIG. 10. Ejected matter over time for the six EoSs considered in this work. The rapid rise is generated by the fast-moving ejecta, while the increase in $M_{\rm ej}$ at late times is caused by the slow-moving tail of the distribution of ejected matter.

estimate that the error in our reported values of $M_{\rm ej}$ is $\sim 150\%$ (see Appendix C for further details). Higher resolution is necessary for more accurate estimates.

As shown in Fig. 10, we find that $M_{\rm ej}$ varies from $\sim 1.0-1.3 \times 10^{-2}~M_{\odot}$ for the M^* -evolutions, which implies a range much smaller than our estimated error. Thus, although we do find some dependence of $M_{\rm ej}$ on the M^* -parameters, the differences are not numerically significant, at least for the particular cold EoS, binary parameters, and resolutions explored here. In contrast, there is a factor-of-8 difference between $M_{\rm ej}$ for the $\Gamma_{\rm th}=1.5$ and $\Gamma_{\rm th}=2$ evolutions, with the latter producing significantly less ejecta.

In [86] it was previously found that larger Γ_{th} can lead to suppressed ejecta. In that work, the authors suggested that M_{ej} depends on Γ_{th} in two competing ways. On the one hand, a larger value of Γ_{th} leads to more efficient shock heating, which acts to increase the amount of matter ejected. However, the remnant is also less compact for large Γ_{th} and, accordingly, has a slower rotational velocity (as shown in our Figs. 7 and 8). This reduces the torque that the remnant exerts onto the surrounding material and, as a result, less matter becomes unbound [86]. Thus, somewhat counterintuitively, a large Γ_{th} can indeed lead to suppressed ejecta. We leave further analysis of the properties of the ejecta to future work.

VI. CONCLUSIONS

In this paper, we have implemented a new prescription for studying finite-temperature effects in binary neutron star mergers, using a two-parameter approximation of the particle effective mass. This is the first implementation of parametric finite-temperature effects that include the effects of degeneracy and that can be added to any cold EoS, in a compact binary merger simulation. We tested this new prescription in rotating, single stars that are initially cold or that initially have a nonzero temperature gradient, as well as in several binary evolutions, and we find that the EoS can support stable stars over long timescales.

We also performed a parameter study to explore a broad range of M^* values in a series of NSNS merger simulations. We considered four sets of M^* -parameters, as well as two constant- $\Gamma_{\rm th}$ values in order to provide a basis of comparison for the new M^* results. While the inspiral portion of the merger is virtually identical for all six thermal treatments, we find significant differences in the postmerger evolution for the different thermal prescriptions. Depending on the thermal treatment, we find up to an order of magnitude difference in the characteristic $P_{\rm th}/P_{\rm cold}$ at core densities just after the merger. As a result of these differences in the postmerger thermal profiles, the mass distribution of the remnant can also vary significantly by the end of our simulations.

Perhaps most interestingly, from an observational point of view, are the differences that can emerge in the postmerger GW signal. We find that the postmerger GW strain is sensitive to the particular choice of M^* -parameters. We plan to further study this dependence in future work. If the postmerger GW spectrum does indeed depend on the parameters of M^* , as our findings hint at, then observations of postmerger GWs may one day offer a new window into the properties of dense matter at nonzero temperatures.

Finally, it is worth noting that the relative importance of thermal effects may change for binaries with different total mass, mass ratio, underlying cold EoS (and, hence, stellar compactness), and potentially also with the added presence of magnetic fields. For example, we expect that the dependence of merger properties on the M^* -parameters will become stronger for softer EoSs, which predict more compact stars. More compact stars are expected to collide at higher velocities, leading to stronger shock heating and an enhanced thermal pressure. Combined with the lower cold pressure of the softer EoS, we expect the thermal pressure may play a more important role in such mergers. We leave the study of such effects to future work.

ACKNOWLEDGMENTS

We are indebted to Antonios Tsokaros for permission to use initial data he generated with the COCAL code for other projects. We are grateful to William East and Frans Pretorius for providing us with their generic primitives recovery routine. We would like to thank Dimitrios Psaltis, Gabriele Bozzola, Erik Wessel, Ryan Westernacher-Schneider, and Elias Most for useful conversations related to this work. C. R. was partially supported during this project by NSF Graduate Research Fellowship Grant No. DGE-1746060, as well as by a joint postdoctoral fellowship at the Princeton Center for Theoretical Science, the Princeton Gravity Initiative, and as a John N. Bahcall Fellow at the Institute for Advanced Study. This research was in part supported by NSF Grant No. PHY-1912619 to the University of Arizona and by NSF PIRE grant No. 1743747. The simulations presented in this work were carried out in part on the Ocelote and ElGato clusters at the University of Arizona, as well as on the Stampede2 cluster at the Texas Advanced Computing Center, under XSEDE allocation PHY190020.

APPENDIX A: LOW-DENSITY DESCRIPTION OF MATTER

While high-density nuclear matter is uniform, matter at densities below $0.5n_{\rm sat}$ can cluster into light and even heavy nuclei. Fermi Liquid Theory, in its standard form, cannot describe the formation of bound states and thus does not accurately capture this regime. (For one approach incorporating the formation of light clusters into Fermi Liquid

Theory, see [32]). In this Appendix, we describe how this limitation affects the M^* -framework in the low-density regime.

The baryon number density, which is the conserved quantity that enters the evolution equations, is given by

$$n_b \equiv \frac{N_n + N_p + \sum A N_{A,Z}}{V} \tag{A1}$$

where N_n and N_p are the number of unbound neutrons and protons, respectively, $N_{A,Z}$ is the number of nuclei with atomic number and charge (A,Z), and V is the volume of the system. If there are nuclei present, n_b differs from the density of effective particles,

$$n_{\text{eff}} \equiv \frac{N_n + N_p + \sum N_{A,Z}}{V}.$$
 (A2)

The particle and baryon density are related by

$$n_b = \langle B \rangle n_{\text{eff}},$$
 (A3)

where $\langle B \rangle$ is the average number of baryons per particle. In the limit of uniform nuclear matter, $\langle B \rangle = 1$; this number increases with the formation of increasingly heavy nuclei.

For a general system of $N_{\rm eff}$ particles, of which some may be bound nuclei, the total thermal energy is given by $U_{\rm th}=\frac{3}{2}TN_{\rm eff}$, via equipartition. The thermal energy per baryon and thermal pressure are thus

$$E_{\rm th} = \left(\frac{3}{2}k_BT\right)\frac{n_{\rm eff}}{n_b} = \left(\frac{3}{2}k_BT\right)\frac{1}{\langle B\rangle}$$
 (A4a)

$$P_{\rm th} = n_{\rm eff} k_B T = \frac{n_b k_B T}{\langle B \rangle}.$$
 (A4b)

In the original RÖP framework, it was assumed that $\langle B \rangle = 1$ at all densities, for simplicity. This approximation introduces some error into calculations of $E_{\rm th}(n,T)$ and $P_{\rm th}(n,T)$ at densities below $0.5n_{\rm sat}$ and at low temperatures $(T \lesssim 1 \ {\rm MeV})$. At higher T, which is the focus of that framework, the nuclei dissociate and $\langle B \rangle \approx 1$ again. We note that, in merger simulations, the temperatures at densities below $0.5n_{\rm sat}$ are typically much larger than 1 MeV (see, e.g., Fig. 6) and that there is little matter at these densities to affect the dynamics of the evolution or the gravitational wave emission. Thus, the impact of this approximation should, in general, be small; but it may become important when considering properties governed by the low-density EoS, such as the ejecta.

In the numerical implementation used in this paper, we take another approach, in which we do not calculate $E_{th}(n,T)$ and $P_{th}(n,T)$ at fixed temperatures. Rather, we exclusively calculate P(E) and E(P) (see Sec. IVA). As a result, the factors of $\langle B \rangle$ in Eqs. (A4) cancel out, and we

recover the correct description of the pressure and energy in this low-density regime. In other words, although we do not explicitly model the presence of nuclei at low-densities, the evolutions are not affected by this approximation.

APPENDIX B: SINGLE STAR TEST RESULTS

In this Appendix, we describe the key results from our single star evolutions in dynamical spacetimes. For both zero-temperature single stars and single stars initialized

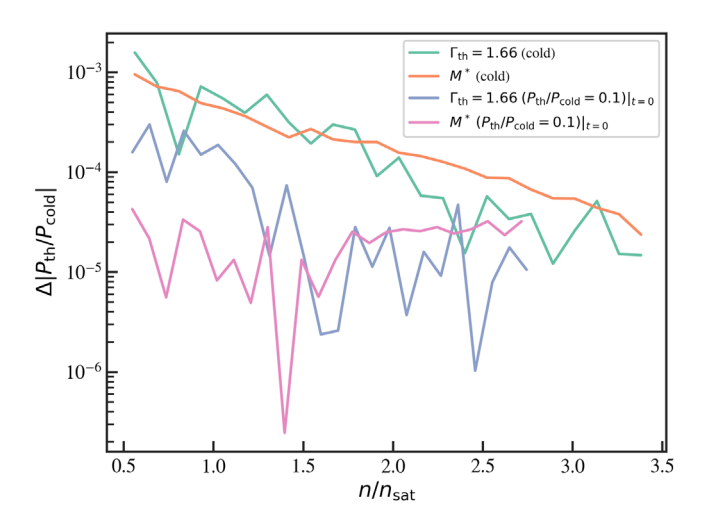


FIG. 11. Total change in the characteristic thermal pressure at each density, between the initial and final time steps (i.e., $|P_{\rm th}/P_{\rm cold}(t=0)-P_{\rm th}/P_{\rm cold}(5t_{\rm dyn})|$). All profiles correspond to the highest-resolution evolutions. Both the hybrid and M^* evolutions maintain the initial thermal profile to within $\lesssim 1$ part in 10^3 at supranuclear densities, for both zero- and finite-temperature initial data.

with $P_{\rm th}/P_{\rm cold}=0.1$, we perform evolutions for $\sim 5t_{\rm dyn}$, where $t_{\rm dyn}=1/\sqrt{\rho_{b,c}}$ is the dynamical timescale and $\rho_{b,c}$ is the central rest mass density. Each set of initial data is evolved with the hybrid approximation with $\Gamma_{\rm th}=1.66$, as well as with the M^* -thermal treatment with $n_0=0.12~{\rm fm}^{-3}$ and $\alpha=0.8$.

While the hybrid EoS has been well tested within the Illinois spacetime + GRMHD code in previous studies [e.g., [47,87]], we include the test results here again, in order to validate our implementation of the primitive recovery scheme of [55] into our code, as well as to provide a basis of comparison for the M^* -EoS results.

For both single star tests, we find that the M^* -EoS is able to maintain the initial thermal profile, with no evidence of spurious heating. Figure 11 shows the change in the characteristic value of $P_{\rm th}/P_{\rm cold}$ from the beginning to the end of the simulation, for each of the single star tests considered. We calculate the characteristic value of $P_{\rm th}/P_{\rm cold}$ in each density bin at each time, as in Sec. V B. Over the ~5 dynamical timescales that were evolved, $P_{\rm th}/P_{\rm cold}$ changes by $\lesssim 10^{-3}$ at supranuclear densities. Additionally, we find that the M^* -EoS performs comparably well to the hybrid approximation at maintaining either a zero-temperature or fixed thermal profile.

In order to monitor the stability of the stars, we track the time-evolution of the quantity, $\Delta \rho_{b,c}$, which represents the change in central rest mass density relative to the value at t=0, and which is expected to converge to zero at second-order with increasing resolution. We show this quantity in Fig. 12 for the zero-temperature evolutions (left panel) and constant $P_{\rm th}/P_{\rm cold}$ thermal profile (right panel). In both cases, the low-resolution quantities have been scaled to show 2nd-order convergence.

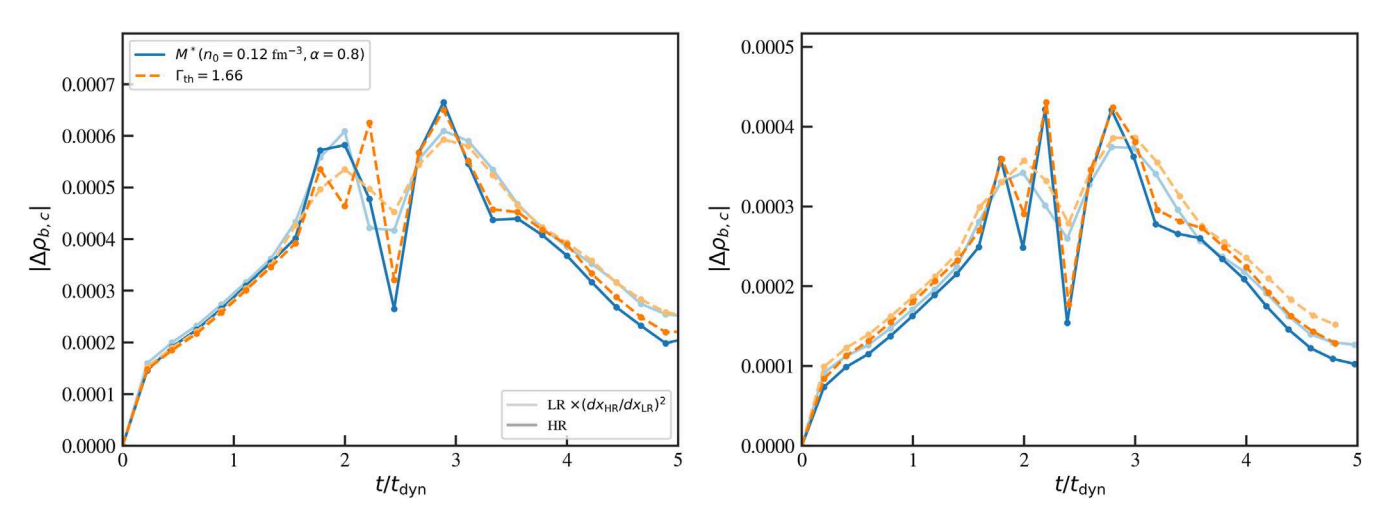


FIG. 12. Left: change in the central rest mass density over five dynamical timescales, for the cold rotating star tests. The blue line represents the tests evolved with the M^* -EoS, while the orange dashed line represents the hybrid evolution. The lighter shade corresponds to the low-resolution evolution (which has been scaled to show 2nd-order convergence), while the darker shade indicates the high-resolution evolution. Right: same as the left panel, but for the rotating star tests with a nonzero initial temperature profile set by $P_{\rm th}/P_{\rm cold}=0.1$. The convergence behavior is identical to the cold evolution.

We find the anticipated 2nd-order convergence in $\Delta \rho_{b,c}$ over time, in both the cold and finite-temperature evolutions. The results are virtually indistinguishable between the M^* and hybrid evolutions, thus providing additional validation of the numerical implementation of the M^* -EoS.

APPENDIX C: RESOLUTION STUDY FOR BINARY EVOLUTIONS

We now present the results of the resolution study for the NSNS merger simulations, evolved with the M^* -EoS with $n_0 = 0.08$ fm⁻³ and $\alpha = 1.3$. The baseline (low) resolution is described in Sec. IV C; the medium resolution is $1.5625 \times$ finer; and the high resolution is $2 \times$ the baseline resolution. These resolutions correspond to ~ 100 , 156, and 200 grid points across the diameter of each initial star, respectively.

Figure 13 shows the convergence of the L2 norm of the Hamiltonian constraint in the left panel, as well as the self-convergence of the amplitude and the phase of ψ_4 in the middle and right panels, respectively. The Hamiltonian constraint violation is expected to converge to zero, with increasing resolution. For the amplitude and the phase of ψ_4 , we determine if there is self-convergence by comparing to the highest- resolution evolution. Self-convergence at second-order requires

$$\frac{Q_{LR} - Q_{HR}}{Q_{MR} - Q_{HR}} = \frac{(\Delta x_{LR} / \Delta x_{HR})^2 - 1}{(\Delta x_{MR} / \Delta x_{HR})^2 - 1},$$
 (C1)

where Q is the quantity of interest; LR, MR, and HR indicate low, medium, and high resolutions, respectively; and Δx is the grid spacing of each resolution. Rearranging this expression, second-order convergence equivalently implies

$$(Q_{LR} - Q_{HR})[(\Delta x_{MR}/\Delta x_{HR})^2 - 1]$$

= $(Q_{MR} - Q_{HR})[(\Delta x_{LR}/\Delta x_{HR})^2 - 1].$ (C2)

These scaled, differential quantities are plotted in the middle and right panels of Fig. 13, for the amplitude and phase of Ψ_4 . The left-hand side of Eq. (C2) is plotted in light blue in Fig. 13, while the right-hand side is plotted in dark blue. The degree to which these two sets of lines agree indicates how close the results are to exhibiting second-order convergence.

We find second-order convergence-to-zero in $\|\mathcal{H}\|$ during the inspiral and for the first few milliseconds postmerger. At later times, the convergence order decays significantly. We likewise find second-order convergence in both the amplitude and the phase of ψ_4 during the inspiral, which also decays at late times.

In order to understand the loss of convergence at late times, we performed an additional medium-resolution evolution for the $\Gamma_{th} = 1.5$ EoS. In comparing $\|\mathcal{H}\|$ for the low- and medium-resolution evolutions with the hybrid EoS, we find qualitatively similar behavior to what is shown in the left panel of Fig. 13—with second-order convergence at early times which then disappears within a few milliseconds postmerger. Although the turbulent nature of the postmerger evolution makes it very difficult to achieve convergence postmerger, we suspect that the decay of convergence at late times found for both the hybrid and M^* thermal treatments stems from discontinuities in the piecewise polytropic representation of the cold EoS. This is further supported from the fact that our cold $\Gamma = 2$ isolated stellar evolutions exhibit approximate second order convergence as expected. NSNS merger simulations performed with different codes have also found a lack of convergence in the postmerger phase when modeling the cold EoS with piecewise polytropes [e.g., [88,89]], lending support to the hypothesis that the issue may

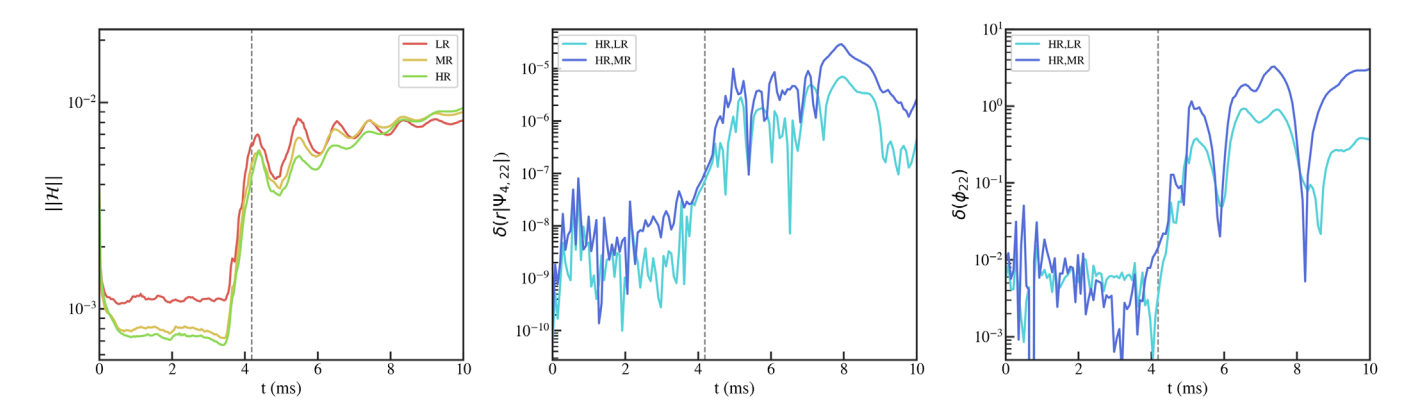


FIG. 13. Left: L2 norm of the Hamiltonian constraint violation, at three different resolutions, for the evolution with M^* -parameters $n_0=0.08~{\rm fm^{-3}}$ and $\alpha=1.3$. Time of merger for the high-resolution evolution is marked with the vertical dashed line ($t_{\rm merger}=4.7~{\rm ms}$). There is second-order convergence during the inspiral and for a short period postmerger, but that convergence decays at later times. Middle: self-convergence of the amplitude of ψ_4 for the $\ell=m=2$ mode, for the same evolution. The results have been scaled to show second-order convergence. Right: self-convergence of the phase of ψ_4 for the $\ell=m=2$ mode, for the same evolution, again scaled to show second-order convergence. As with the Hamiltonian constraint, we find second-order convergence at early times, which disappears after the merger.

stem from the piecewise polytropes. We plan to investigate this issue further in future work.

Finally, we compare the ejecta mass for the low-and high-resolution evolutions in Fig. 14. The differences in the characteristic speed of the fastest ejecta are negligible between the three resolutions studied here. However, the total value of M_{ei} differs more significantly between the resolutions. Because the higher-resolution cases are only evolved for ~10 ms postmerger, we are unable to extract a late-time value for $M_{\rm ej}$ as we did in Sec. V. However, $M_{\rm ej}$ is starting to asymptote at 10 ms postmerger for all three resolutions, thereby allowing us to make a reasonable comparison. The values of M_{ei} extracted in this way indicate 1.5-order convergence. We note that, although the overall convergence of the code decays at late times after the merger, the ejecta are launched at the merger and, hence, still exhibit convergence and can be used to make a reasonable error estimate. We find a fractional error between the low- and high- resolution values of $\sim 150\%$.

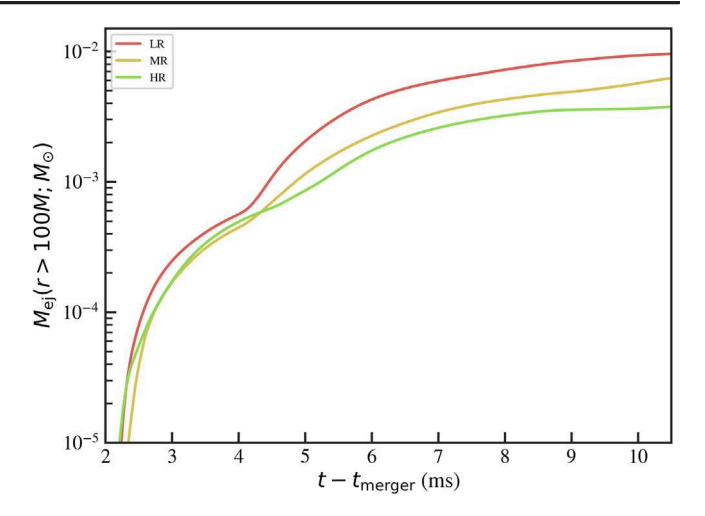


FIG. 14. Ejecta mass for the low-, medium-, and high-resolution evolutions for the M^* -EoS with $n_0=0.08~{\rm fm^{-3}}$ and $\alpha=1.3$. At 10 ms postmerger, the fractional difference in $M_{\rm ej}$ is ~150% between the lowest and highest resolutions.

- B. P. Abbott, R. Abbott, T. D. Abbott, F. Acernese, K. Ackley, C. Adams, T. Adams, P. Addesso, R. X. Adhikari, V. B. Adya *et al.*, Phys. Rev. Lett. **119**, 161101 (2017).
- [2] B. P. Abbott, R. Abbott, T. D. Abbott, S. Abraham, F. Acernese, K. Ackley, C. Adams, R. X. Adhikari, V. B. Adya, C. Affeldt *et al.*, Astrophys. J. Lett. **892**, L3 (2020).
- [3] L. Baiotti, Prog. Part. Nucl. Phys. 109, 103714 (2019).
- [4] C. A. Raithel, Eur. Phys. J. A 55, 80 (2019).
- [5] K. Chatziioannou, Gen. Relativ. Gravit. 52, 109 (2020).
- [6] L. Baiotti and L. Rezzolla, Rep. Prog. Phys. 80, 096901 (2017).
- [7] V. Paschalidis and N. Stergioulas, Living Rev. Relativity 20, 7 (2017).
- [8] R. Oechslin, H.-T. Janka, and A. Marek, Astron. Astrophys. **467**, 395 (2007).
- [9] L. Baiotti, B. Giacomazzo, and L. Rezzolla, Phys. Rev. D 78, 084033 (2008).
- [10] A. Bauswein, H.-T. Janka, and R. Oechslin, Phys. Rev. D 82, 084043 (2010).
- [11] A. Bauswein, R. Oechslin, and H. T. Janka, Phys. Rev. D **81**, 024012 (2010).
- [12] Y. Sekiguchi, K. Kiuchi, K. Kyutoku, and M. Shibata, Phys. Rev. Lett. 107, 051102 (2011).
- [13] V. Paschalidis, Z. B. Etienne, and S. L. Shapiro, Phys. Rev. D 86, 064032 (2012).
- [14] J. M. Lattimer and M. Prakash, Astrophys. J. **550**, 426 (2001).
- [15] F. Özel and P. Freire, Annu. Rev. Astron. Astrophys. 54, 401 (2016).
- [16] J. M. Lattimer and D. F. Swesty, Nucl. Phys. A535, 331 (1991).
- [17] H. Shen, H. Toki, K. Oyamatsu, and K. Sumiyoshi, Nucl. Phys. **A637**, 435 (1998).

- [18] M. Hempel and J. Schaffner-Bielich, Nucl. Phys. A837, 210 (2010).
- [19] S. Typel, M. Oertel, and T. Klähn, Phys. Part. Nuclei 46, 633 (2015).
- [20] M. Oertel, M. Hempel, T. Klähn, and S. Typel, Rev. Mod. Phys. 89, 015007 (2017).
- [21] T. Fischer, M. Hempel, I. Sagert, Y. Suwa, and J. Schaffner-Bielich, Eur. Phys. J. A 50, 46 (2014).
- [22] H.-T. Janka, T. Zwerger, and R. Moenchmeyer, Astron. Astrophys. **268**, 360 (1993).
- [23] C. Constantinou, B. Muccioli, M. Prakash, and J. M. Lattimer, Phys. Rev. C **92**, 025801 (2015).
- [24] C. A. Raithel, F. Özel, and D. Psaltis, Astrophys. J. **875**, 12 (2019).
- [25] A. Figura, J.-J. Lu, G. F. Burgio, Z.-H. Li, and H. J. Schulze, Phys. Rev. D 102, 043006 (2020).
- [26] G. Baym and C. Pethick, *Landau FermiLiquid Theory:* Concepts and Applications (Wiley, New York, 1991).
- [27] C. Constantinou, B. Muccioli, M. Prakash, and J.M. Lattimer, Ann. Phys. (Amsterdam) **363**, 533 (2015).
- [28] C. M. Varma, Z. Nussinov, and W. van Saarloos, Phys. Rep. **361**, 267 (2002).
- [29] A. Gerhold, A. Ipp, and A. Rebhan, Phys. Rev. D 70, 105015 (2004).
- [30] T. Schäfer and K. Schwenzer, Phys. Rev. D 70, 114037 (2004).
- [31] K. Schwenzer, arXiv:1212.5242.
- [32] G. Röpke, D. N. Voskresensky, I. A. Kryukov, and D. Blaschke, Nucl. Phys. A970, 224 (2018).
- [33] A. S. Schneider, L. F. Roberts, and C. D. Ott, Phys. Rev. C 96, 065802 (2017).
- [34] J. W. Holt, N. Kaiser, and T. R. Whitehead, Phys. Rev. C **97**, 054325 (2018).

- [35] Y. Lim and J. W. Holt, arXiv:1909.09089.
- [36] A. Carbone and A. Schwenk, Phys. Rev. C 100, 025805 (2019).
- [37] S. Huth, C. Wellenhofer, and A. Schwenk, Phys. Rev. C 103, 025803 (2021).
- [38] J. Keller, C. Wellenhofer, K. Hebeler, and A. Schwenk, Phys. Rev. C 103, 055806 (2021).
- [39] A. W. Steiner, J. M. Lattimer, and E. F. Brown, Astrophys. J. Lett. 765, L5 (2013).
- [40] G. Shen, C. J. Horowitz, and S. Teige, Phys. Rev. C 83, 035802 (2011).
- [41] C. Palenzuela, S. L. Liebling, D. Neilsen, L. Lehner, O. L. Caballero, E. O'Connor, and M. Anderson, Phys. Rev. D 92, 044045 (2015).
- [42] D. Radice, F. Galeazzi, J. Lippuner, L. F. Roberts, C. D. Ott, and L. Rezzolla, Mon. Not. R. Astron. Soc. 460, 3255 (2016).
- [43] L. Lehner, S. L. Liebling, C. Palenzuela, O. L. Caballero, E. O'Connor, M. Anderson, and D. Neilsen, Classical Quantum Gravity 33, 184002 (2016).
- [44] F. Foucart, E. O'Connor, L. Roberts, L. E. Kidder, H. P. Pfeiffer, and M. A. Scheel, Phys. Rev. D 94, 123016 (2016).
- [45] L. Bovard, D. Martin, F. Guercilena, A. Arcones, L. Rezzolla, and O. Korobkin, Phys. Rev. D 96, 124005 (2017).
- [46] E. R. Most, L. J. Papenfort, V. Dexheimer, M. Hanauske, S. Schramm, H. Stöcker, and L. Rezzolla, Phys. Rev. Lett. 122, 061101 (2019).
- [47] Z. B. Etienne, V. Paschalidis, R. Haas, P. Mösta, and S. L. Shapiro, Classical Quantum Gravity 32, 175009 (2015).
- [48] G. Allen, D. Angulo, I. Foster, G. Lanfermann, C. Liu, T. Radke, E. Seidel, and J. Shalf, Int. J. High Performance Comput. Appl. 15, 345 (2001).
- [49] E. Schnetter, S. H. Hawley, and I. Hawke, Classical Quantum Gravity 21, 1465 (2004).
- [50] E. Schnetter, P. Diener, E. N. Dorband, and M. Tiglio, Classical Quantum Gravity 23, \$553 (2006).
- [51] M. Shibata and T. Nakamura, Phys. Rev. D **52**, 5428 (1995).
- [52] T. W. Baumgarte and S. L. Shapiro, Phys. Rev. D 59, 024007 (1998).
- [53] C. Bona, J. Massó, E. Seidel, and J. Stela, Phys. Rev. Lett. 75, 600 (1995).
- [54] M. Alcubierre, B. Brügmann, P. Diener, M. Koppitz, D. Pollney, E. Seidel, and R. Takahashi, Phys. Rev. D 67, 084023 (2003).
- [55] W. E. East, F. Pretorius, and B. C. Stephens, Phys. Rev. D 85, 124010 (2012).
- [56] C. A. Raithel, F. Ozel, and D. Psaltis, Astrophys. J. 915, 73 (2021).
- [57] S. Rosswog, E. Ramirez-Ruiz, and M. B. Davies, Mon. Not. R. Astron. Soc. 345, 1077 (2003).
- [58] M. B. Tsang, Y. Zhang, P. Danielewicz, M. Famiano, Z. Li, W. G. Lynch, and A. W. Steiner, Phys. Rev. Lett. 102, 122701 (2009).

- [59] A. W. Steiner, J. M. Lattimer, and E. F. Brown, Astrophys. J. 722, 33 (2010).
- [60] C. Xu and B.-A. Li, arXiv:1104.2075.
- [61] I. Vidaña, A. Polls, and C. Providência, Phys. Rev. C 84, 062801 (2011).
- [62] A. Lovato, O. Benhar, S. Fantoni, A. Y. Illarionov, and K. E. Schmidt, Phys. Rev. C 83, 054003 (2011).
- [63] A. Carbone, A. Polls, and A. Rios, Europhys. Lett. 97, 22001 (2012).
- [64] A. Rios, A. Polls, and W. H. Dickhoff, Phys. Rev. C 89, 044303 (2014).
- [65] O. Hen, B.-A. Li, W.-J. Guo, L. B. Weinstein, and E. Piasetzky, Phys. Rev. C 91, 025803 (2015).
- [66] A. W. Steiner, M. Hempel, and T. Fischer, Astrophys. J. 774, 17 (2013).
- [67] G. B. Cook, S. L. Shapiro, and S. A. Teukolsky, Astrophys. J. 424, 823 (1994).
- [68] G. B. Cook, S. L. Shapiro, and S. A. Teukolsky, Astrophys. J. 422, 227 (1994).
- [69] K. Uryū and A. Tsokaros, Phys. Rev. D **85**, 064014 (2012).
- [70] A. Tsokaros, K. Uryū, and L. Rezzolla, Phys. Rev. D 91, 104030 (2015).
- [71] A. Tsokaros, K. Uryū, M. Ruiz, and S. L. Shapiro, Phys. Rev. D 98, 124019 (2018).
- [72] L. Engvik, M. Hjorth-Jensen, E. Osnes, G. Bao, and E. Østgaard, Phys. Rev. Lett. 73, 2650 (1994).
- [73] L. Engvik, E. Osnes, M. Hjorth-Jensen, G. Bao, and E. Ostgaard, Astrophys. J. 469, 794 (1996).
- [74] J. S. Read, B. D. Lackey, B. J. Owen, and J. L. Friedman, Phys. Rev. D 79, 124032 (2009).
- [75] P. B. Demorest, T. Pennucci, S. M. Ransom, M. S. E. Roberts, and J. W. T. Hessels, Nature (London) 467, 1081 (2010).
- [76] J. Antoniadis, P. C. C. Freire, N. Wex et al., Science 340, 1233232 (2013).
- [77] E. Fonseca, T. T. Pennucci, J. A. Ellis, I. H. Stairs, D. J. Nice, S. M. Ransom, P. B. Demorest, Z. Arzoumanian, K. Crowter, T. Dolch, R. D. Ferdman, M. E. Gonzalez, G. Jones, M. L. Jones, M. T. Lam, L. Levin, M. A. McLaughlin, K. Stovall, J. K. Swiggum, and W. Zhu, Astrophys. J. 832, 167 (2016).
- [78] H. T. Cromartie et al., Nat. Astron. 4, 72 (2020).
- [79] C. Reisswig and D. Pollney, Classical Quantum Gravity 28, 195015 (2011).
- [80] A. S. Schneider, L. F. Roberts, C. D. Ott, and E. O'Connor, Phys. Rev. C 100, 055802 (2019).
- [81] H. Yasin, S. Schäfer, A. Arcones, and A. Schwenk, Phys. Rev. Lett. **124**, 092701 (2020).
- [82] W. E. East, V. Paschalidis, F. Pretorius, and A. Tsokaros, Phys. Rev. D 100, 124042 (2019).
- [83] A. Bauswein and N. Stergioulas, J. Phys. G **46**, 113002 (2019).
- [84] J. A. Clark, A. Bauswein, N. Stergioulas, and D. Shoemaker, Classical Quantum Gravity 33, 085003 (2016).
- [85] H. Yang, V. Paschalidis, K. Yagi, L. Lehner, F. Pretorius, and N. Yunes, Phys. Rev. D 97, 024049 (2018).

- [86] K. Hotokezaka, K. Kiuchi, K. Kyutoku, H. Okawa, Y.-i. Sekiguchi, M. Shibata, and K. Taniguchi, Phys. Rev. D 87, 024001 (2013).
- [87] Z. B. Etienne, Y. T. Liu, and S. L. Shapiro, Phys. Rev. D **82**, 084031 (2010).
- [88] V. Paschalidis, W. E. East, F. Pretorius, and S. L. Shapiro, Phys. Rev. D **92**, 121502 (2015).
- [89] W. E. East, V. Paschalidis, F. Pretorius, and S. L. Shapiro, Phys. Rev. D 93, 024011 (2016).